Zebrafish differentially process colour across visual space to match natural scenes

Maxime JY Zimmermann*[1], Noora E Nevala*[1], Takeshi Yoshimatsu*[1],

Daniel Osorio[1], Dan-Eric Nilsson[2], Philipp Berens[3,4,5] and Tom Baden[1,3$]

1: School of Life Sciences, University of Sussex, UK

2: Lund Vision Group, University of Lund, Sweden

3: Institute of Ophthalmic Research, University of Tübingen, Germany

4: Bernstein Centre for Computational Neuroscience, University of Tübingen, Germany

5: Centre for Integrative Neuroscience, University of Tübingen, Germany

*equal contribution

$Correspondence at t.baden@sussex.ac.uk

7 colour figures (main) and 4 colour figures (supplement), 3 Supplementary Data sheets

Words: 5737 (Main incl. abstract), 2380 (Methods), 1596 (Legends), 1281 (Supplement)

Abbreviations used. AC: Amacrine Cell; BC: Bipolar Cell; BIC: Bayesian Information Criterion; ChAT: Choline acetyltransferase; *dpf*: days postfertilisation; GCL: Ganglion Cell Layer; GFP: Green Fluorescent Protein; HC: Horizontal Cell; IPL: Inner Plexiform Layer; INL: Inner Nuclear Layer; LED: Light Emitting Diode; LWS: Long Wavelength Sensitive; MWS: Middle Wavelength Sensitive; PCA: Principal Component Analysis; PKCα: Phosphokinase C alpha; PR: Photoreceptor; RGC: Retinal Ganglion Cell; RGBU: Red-Green-Blue-Ultraviolet; ROI: Region of Interest; OPL: Outer Plexiform Layer; SAC: Starburst Amacrine Cell; s.d.: Standard deviation; s.e.m.: Standard Error of the Mean; SWS: Short Wavelength Sensitive; SZ: Strike Zone; UV: Ultraviolet; UVS: UV Sensitive.

31   **Summary**

32   Animal eyes evolve to process behaviourally important visual information, but how retinas

33   deal with statistical asymmetries in visual space remains poorly understood. Using

34   hyperspectral imaging in the field, *in-vivo* 2-photon imaging of retinal neurons and anatomy,

35   here we show that larval zebrafish use a highly anisotropic retina to asymmetrically survey

36   their natural visual world. First, different neurons dominate different parts of the eye, and are

37   linked to a systematic shift in inner retinal function: Above the animal, there is little colour in

38   nature and retinal circuits are largely achromatic. Conversely, the lower visual field and

39   horizon are colour-rich, and are predominately surveyed by chromatic and colour-opponent

40   circuits that are spectrally matched to the dominant chromatic axes in nature. Second, above

41   the frontal horizon, a high-gain ultraviolet-system piggy-backs onto retinal circuits, likely to

42   support prey-capture. Our results demonstrate high functional diversity among single

43   genetically and morphologically defined types of neurons.

44

Main

Sensory systems have evolved to serve animals' behavioural requirements. They are tuned to prioritise behaviourally important computations subject to constraints on the neural hardware and metabolic cost (Land & Nilson 2012; Cronin et al. 2014). In vision, specialisations are often made according to the statistics of specific regions in visual space. For example, mouse cones preferentially process dark contrasts above but not below the visual horizon, likely boosting the detection of aerial predators (Baden et al. 2013; Yilmaz & Meister 2013; Calderone & Jacobs 1995). However, beyond anisotropic receptor distributions, systematically linking the statistics of the visual world to the properties of visual systems has been difficult (Lewis & Zhaoping 2006; Ruderman et al. 1998; Webster & Mollon 1997; Buchsbaum & Gottschalk 1983; Simoncelli & Olshausen 2001). Making a link of this kind ideally requires an animal model that allows *in vivo* measurements of light-driven neuronal activity in any part of the eye. In addition, it is necessary to measure the visual characteristics of the animal's natural world (Dyakova & Nordström 2017), and focus on aspects that are behaviourally important yet sufficiently low-dimensional to be amenable to statistical evaluation. One model that meets these criteria is the colour vision system of the larval zebrafish.

Within three days of hatching, larval zebrafish become highly visual animals with tetrachromatic wide-angle vision (Wong & Dowling 2005; Mehta et al. 2013; Easter, Jr. & Nicola 1996) and well-studied visual behaviours (Preuss et al. 2014; Trivedi & Bollmann 2013; Semmelhack et al. 2014; Temizer et al. 2015; Dunn et al. 2016; Bianco et al. 2011; Muto & Kawakami 2013; Avdesh et al. 2010; Mueller & Neuhauss 2014). Vision is metabolically costly for larval zebrafish: the two eyes make up nearly a quarter of the total body volume, with the neuronal retina taking up >75% of each eye. Indeed, about half of the larva's central neurons are located inside the eyes (Supplementary Discussion). Space limitations and energy demand create strong evolutionary pressure to make the best use of every visual neuron – potentially driving regional specialisations within the eye. Here, we

3

72 examine how larval zebrafish retinal circuits process chromatic information in the immediate

73 context of their natural visual world and their behavioural demands. Throughout, we used

74 zebrafish larvae at 7-8 days post fertilisation, *dpf* (for discussion on the choice of age see

75 Supplementary Materials). We find that the eye is functionally and anatomically extremely

76 anisotropic, and these anisotropies match an asymmetrical distribution of colour in the

77 zebrafish natural habitat.

78

Chromatic content in nature varies with visual elevation

80 Zebrafish are surface dwelling freshwater fish of the Indian subcontinent (Arunachalam et al.

81 2013; Parichy 2015; Spence et al. 2008). Larval and juvenile zebrafish live mostly in shallow,

82 low current pockets on the sides of streams and rice paddies – probably to avoid predation

83 by larger fish (Engeszer et al. 2007), to conserve energy and to facilitate visually guided prey

84 capture of aquatic microorganisms such as paramecia (Semmelhack et al. 2014; Bianco et

85 al. 2011; Preuss et al. 2014; Muto et al. 2017). To systematically record how the visual world

86 varies with elevation in the zebrafish natural habitat we used two complementary

87 approaches: (i) an action camera to take underwater 180° wide-angle, high spatial resolution

88 photographs (Fig. 1-e) and (ii) a custom-built hyperspectral scanner (Baden et al. 2013;

89 Nevala et al. 2017) to take 60° full-spectrum images at a lower spatial resolution, matched to

90 that of the larval zebrafish (Fig. 1f-l). We surveyed n=31 scenes from six field sites in West

91 Bengal, India (SFig. 1a,b, Supplementary Data).

92 The action camera data demonstrated that in these shallow (<50 cm) waters, both the

93 substrate and the water surface are simultaneously viewed by the larvae's wide-angle eyes

94 (Fig. 1a), and that the spectrum of light varies strongly with elevation. Directly ahead and to

95 the sides zebrafish eyes align with a mid-wavelength- ("green") dominated underwater

96 horizon which divides a long-wavelength- ("red") biased lower visual field and a short-

97 wavelength- ("blue") biased upper visual field of the ground reflecting the underside of the

98 water surface (Fig. 1a, SFig. 1 b-d). Beyond ~42° elevation, this reflection gives way to

99 Snell's window (Jerlov 1976; Janssen 1981) – a short-wavelength-biased representation of

100 the 180° world above the water surface compressed into a constant ~97° of visual angle

101 directly above the animal. To estimate which part of the scene contained most chromatic

102 information, we used principal component analysis, using red, green and blue (RGB) pixel

103 values from different elevations. As in terrestrial scenes (Lewis & Zhaoping 2006), PC1

104 reliably captured the achromatic component where the R, G and B channels co-vary (Fig.

105 1b). Across the entire image, this component always explained >90% of the total variance.

106 Next, PC2 and PC3 captured the main chromatic axes (red versus blue; green versus blue)

107 in decreasing order of importance (Fig. 1c,d). Further analysis revealed that the horizon and

108 lower visual field accounted for most chromatic structure, while Snell's window above the

109 animal was effectively achromatic (Fig. 1e). For this, we horizontally divided each of n=31

110 images into 5° stripes and calculated the fraction of the total image variance explained by

111 PC2 and PC3 as a function of elevation (Fig. 1e). As our camera was designed for human

112 trichromacy, and can therefore only approximate the spectral content available to the

113 zebrafish's tetrachromatic retina (Chinen et al. 2003; Endeman et al. 2013), we next

114 computed the chromatic image statistics in hyperspectral images taken at the same sites as

115 seen by the larval zebrafish.

116

Spectral positioning of zebrafish cone-opsins under natural light

118 To sample full-spectrum underwater images in the zebrafish natural world, we custom built a

119 hyperspectral scanner (Baden et al. 2013) comprising a spectrometer and two mirrors

120 mounted on Arduino-controlled servo-motors (Fig. 1f) (Nevala et al. 2017). The system

121 collected 60° full spectrum (200-1000 nm) images centred on the underwater horizon.

122 Individual readings were regularly spaced at ~1.6° to approximate the behavioural resolution

123 limit of larval zebrafish (Haug et al. 2010). A total of 31 scans of 1,000 "pixels" each were

124 taken at the same scenes previously photographed with our action camera (Supplementary

125 Data). To estimate what spectral content is available in nature for zebrafish vision, we

126 multiplied the mean of all 31,000 spectra with the animal's cone absorption spectra.

127 Zebrafish larvae express mainly four opsins in their four cone types: LWS (548nm), MWS

128 (467 nm), SWS (411 nm) and UVS (365 nm) (Chinen et al. 2003) (for discussion see

129 Supplementary Materials). For simplicity, we will refer to these as the "red" (R), "green" (G),

130 "blue" (B) and "ultraviolet" (U) channels, respectively. As expected (Morris et al. 1995; Chiao

131 et al. 2000), short-wavelengths from the sky illumination were attenuated in the water,

132 resulting in a red-shift of the available light (Fig. 1g). The peak of the mean underwater-

133 spectrum aligned with the absorbance peak of the zebrafish R-opsin (Fig. 1h), suggesting

134 that R-cones are strongly driven in the zebrafish's natural habitat, and are thus well suited to

135 encode features that require high signal-to-noise representation, such as movement

136 (Schaerer & Neumeyer 1996). In contrast, U-cones lay at the extreme short-wavelength end

137 of available light under water. In this regime, the signal power is ~7% compared to the red

138 channel. Investing neural resources despite the low signal power suggests that zebrafish

139 gain important benefits from using this channel. For example, it could aid detecting UV-rich

140 prey (Novales Flamarique 2012; Flamarique 2016) against the water's underside internal

141 reflection (Janssen 1981), boost achromatic contrasts against the underwater horizon (Losey

142 et al. 1999; Nava et al. 2011) and more generally to support detection of chromatic contrast.

143 Finally. B- (16%) and G-cones (45%) received intermediate number of photons, and are

144 likely used for both achromatic and chromatic computations alongside the other cones.

145

Short-vs-long wavelength computations carry most chromatic information

147 We next asked which chromatic contrasts in RGBU opsin space predominate in the natural

148 environment of the zebrafish larvae. For this, we multiplied the spectrum of each "pixel" with

149 the spectral sensitivity function of each opsin to yield four monochromatic opsin activation

150 images from each scan (Fig, 1i,j, SFig. 1f, cf. Fig. 1a), one for each opsin channel. As

151   predicted from the available light, the R-opsin image showed the most spatial structure,

152   followed by G and B. In contrast, the U-opsin image had a "foggy" appearance, probably due

153   to UV-light scattering on dissolved organic matter. Such UV-background light can be

154   exploited by animals to detect the UV-dark silhouettes of otherwise difficult to spot objects

155   (Cronin & Bok 2016; Losey et al. 1999).

156   Next, to separate achromatic and chromatic content across these four opsin images, we

157   computed PCA across now 4-dimensional RGBU opsin space (like above). This again

158   reliably extracted achromatic luminance information into PC1 and then three chromatic

159   dimensions (PC2-4) (Fig. 1k, SFig. 1e). The mean opsin contrasts obtained by PCA across

160   all n=31 scans were (i) RG / BU ("long vs. short wavelength opponency"), (ii) RU / GB and.

161   (iii) RB / GU (complex opponencies). We again cut the images into 5° horizontal stripes and

162   found that the sum of variance explained by the three chromatic dimensions peaked at and

163   below the underwater horizon (Fig. 1l, cf. Fig. 1e).

164   The efficient coding hypothesis (Attneave 1954; Barlow 1961; Simoncelli & Olshausen 2001)

165   predicts that the obtained opsin contrasts should also be encoded by retinal neurons, as is

166   the case for human trichromacy (Buchsbaum & Gottschalk 1983; Lewis & Zhaoping 2006).

167   Moreover, these circuits should be biased to retinal regions that survey the horizon and

168   lower visual field, where these chromatic contrasts predominate (Fig. 1m). In addition,

169   species specific visual demands that cannot emerge from the statistics of static scenes, such

170   as the need for prey capture and to avoid predators, may drive the evolution of additional,

171   dedicated circuits. For example, zebrafish larvae feed on "translucent" unicellular paramecia

172   that scatter light in a UV-biased manner (Spence et al. 2007; Novales Flamarique 2012;

173   Flamarique 2016). For capture, larvae approach their prey from slightly below and converge

174   the eyes to bring their image into binocular space in front of and just above the horizon

175   (Bianco et al. 2011; Patterson et al. 2013), but outside Snell's window (J Semmelhack,

176   personal communication). In this part of visual space, the paramecium is illuminated by its

177   own Snell's window and thus - from point of view of the larval zebrafish - broadcasts its

178 position as a UV-bright spot against the underside of the water (Fig. 1n) (Janssen 1981). For

179 surveying this part of visual space (here dubbed "strike zone", SZ), the larval retina should

180 invest in UV-driven prey capture circuits. Finally, detecting UV-dark silhouettes against a UV-

181 bright background should work across the entire upper visual field including Snell's window.

182 Our natural image data and known behavioural demands of larval zebrafish lead to three

183 predictions for how these animals' retinal circuits should be organised for efficient coding:

184   1) Above the animal, light is short-wavelength biased and there is little colour

185   information, but the visual input can be used to spot silhouettes – accordingly, circuits

186   should be achromatic or short-wavelength biased.

187   2) In the strike zone, the behavioural requirement for prey capture should drive an

188   increased predominance of UV-On circuits.

189   3) Along the horizon, and below the animal, the retina should invest in chromatic

190   circuits, with an emphasis on short- versus long-wavelength computations.

191 We next set out to test these predictions experimentally. We first assess the distributions of

192 retinal neurons across the eye, and subsequently used *in-vivo* functional imaging to study

193 the chromatic organisation of the inner retina.

194

Anisotropic photoreceptor distributions match the distribution of natural light

196 To study the distribution of the zebrafish larvae's four cone- and one rod-photoreceptor types

197 across the retinal surface, we fluorescently labelled individual photoreceptor populations. For

198 R-, B- and U-cones we expressed fluorescent proteins under cone-type specific promotors

199 *thrb*, *sws2* and *sws1*, respectively. No line exclusively labelling G-cones was available.

200 Instead, we calculated their distribution by subtracting genetically defined R-cones from

201 retinae where both R- and G-cones were labelled using immunohistochemistry (zpr-1

202 antibody (Larison & Bremiller 1990)). Finally, rod-photoreceptors (rods) were surveyed by

203 expressing mCherry under rod specific promoter *xops* (Fadool 2003). We projected each 3D

8

204   retina as imaged under a confocal microscope into a local-distance-preserving 2D plane,

205   counted photoreceptors and projected their positions back onto the original semi-sphere to

206   generate density maps of each photoreceptor type across the 3D eye (Fig. 2a, Methods).

207   Unlike in adults, who feature a crystalline photoreceptor mosaic (Engström 1960), in larvae

208   all photoreceptor distributions were anisotropic (Fig. 2b-d). The sum of all cones, which

209   made up ~92% of all photoreceptors, peaked at the horizon (Fig. 2c,d), in line with this part

210   of visual space comprising most chromatic information in nature (Fig. 1e,i). This bias was

211   mainly driven by R-, G-, and B- cones. In contrast, UV-cones peaked ~30º above the forward

212   facing horizon to form a UV-specialised area centralis (Schmitt & Dowling 1999), likely to

213   support visual prey capture (Fig. 1n). Next, the lower visual field was dominated by R-cones,

214   yet closely followed by approximately matched densities all other cones. Like the horizon,

215   this part of visual space could therefore be used for colour vision (Fig. 1m), but with an

216   additional long-wavelength bias as observed in nature (SFig. 1d). In contrast, the upper

217   visual field comprised fewest cones of any type, but instead had an increased number of

218   rods. Unlike cones, rods near exclusively looked straight up through the effectively

219   achromatic but bright Snell's window, or straight down, perhaps to support the detection of

220   optic flow on the ground even in dim light and/or allow telling the distance to the ground for

221   maximal camouflage for predation from above. Accordingly, already at the level of

222   photoreceptor distributions, the retina of larval zebrafish exhibits a series of anisotropies that

223   align well with the major spectral trends in their visual world and their behavioural demands.

224   How are these anisotropies reflected in the inner retina?

225

An anisotropic inner retina

227   To survey inner retinal structure, we immunolabelled the intact eyes of 7-8 *dpf Tg(-*

228   *1.8ctbp2:SyGCaMP6)* larvae against GFP (green, all bipolar cell (BC) terminals (Johnston et

229   al. 2014), ChAT (blue, starburst amacrine cells, SACs (Famiglietti 1983; Nevin et al. 2008))

230   and PKCα (magenta, "On" BCs (Nevin et al. 2008)) and imaged them across the sagittal

231   plane aligned with the back-surface of the lens in the 3D eye (Methods). In larval zebrafish,

232   the full monocular field of view is ~163°, and at rest eyes are rotated forwards by ~18.5°

233   (~35.5° during prey-capture) (Bianco et al. 2011; Patterson et al. 2013). The surveyed

234   sagittal plane samples the visual world in a cone of ~130° (Fig. 2e, SFig. 2), such that its

235   temporal extreme projects in front of the fish while the nasal extreme projects outwards and

236   backwards along the horizon. Dorsal and ventral positions survey the visual world at ~65°

237   elevation below and above the animal, respectively. For simplicity, all visual field coordinates

238   are given in egocentric space from the point of view of the fish: up (ventral), "strike zone"

239   (SZ, temporo-ventral), down (dorsal) and outward horizon (nasal).

240   Our data on inner retinal structure consolidated and extended all large-scale anisotropies

241   set-up by the photoreceptors (Fig. 2f-l). Like cone-densities (Fig. 2c,d), also inner retinal

242   thickness varied nearly two-fold with position, with the thickest inner plexiform layer (IPL)

243   segments aligning with the horizons (Fig. 2f,k). Alongside, the number, distribution, shapes

244   and sizes of synaptic terminals varied with eye position. For example, while PKCα labelling

245   highlighted three strata in the strike zone (one between and two below the ChAT bands, Fig.

246   $2h_2$), circuits surveying the world above the animal appeared to have only the two lower

247   strata (Fig. $2i_2$). Here, the lowest band featured particularly large BC terminals that are

248   characteristic for teleost "mixed" BCs that process inputs from rod-photoreceptors (Stell

249   1967) – in agreement with the anisotropic distribution of rods (Fig. 2c). In addition, there

250   were PKCα negative terminals at the IPL bottom that were restricted to the strike zone (Fig.

251   2h, l). SAC processes also varied with position. For example, the neat bilayer of ChAT

252   immunoreactivity in the strike zone and for looking outward (Figs. $2h_2$, j_2) disappeared into a

253   "haze" in circuits looking down (Fig. $2i_2$, Fig. 2l). Clearly, the larval zebrafish retina features a

254   broad range of anatomical specialisations across the visual field. How are these anatomical

255   specialisations reflected in function? To address this question, we next turned to calcium

256   imaging of BC terminals across the eye.

257

The inner retina is divided into anisotropic chromatic and achromatic layers

259 We used 2-photon *in vivo* imaging of light-driven activity in retinal BCs expressing the

260 calcium biosensor GCaMP6f under the *ctbp2* (*ribeyeA)* promoter fused to the synaptic

261 protein Synaptophysin (Dreosti et al. 2009; Rosa et al. 2016). We focussed on BCs (Euler et

262 al. 2014) as (i) they directly and differentially collect inputs from all photoreceptors to form

263 the basis of colour vision (Li et al. 2012; Behrens, Schubert, Haverkamp, Euler & Berens

264 2016), (ii) they are the only neuron class that contacts all other neurons in the retina and (iii)

265 they directly drive retinal ganglion cells, the eye's connection to the brain. Individual pre-

266 synaptic terminals of BCs can be resolved while imaging the entire depth of the inner retina

267 (Dreosti et al. 2009) (Fig. 3a).

268 To estimate each BC terminal's chromatic sensitivity, we used a tetrachromatic "noise"

269 stimulus (Fig. 3b,c). Specifically, each of four LEDs that were spectrally matched to the

270 absorption peaks of the four cone-opsins (SFig. 3a) were presented to the live larvae

271 through the objective and flickered in a known random binary sequence at 12.8 Hz (Fig. 3b).

272 Using reverse correlation (Chichilnisky 2001), we then recovered four temporal response

273 kernels for each BC terminal (Franke et al. 2017), one for each LED and thus effective cone-

274 type input (Fig. 3c). This revealed different chromatic sensitivities in different BC terminals.

275 For example, some terminals displayed near-equal sensitivity to all four LEDs, indicating a

276 wavelength-invariant response preference (achromatic terminals, Fig. 3a-c, ROI 1). Other

277 terminals had kernels with opposite polarity across LEDs (colour opponent terminals, Fig.

278 3a-c, ROI 2). In an example scan from the "outward horizon" for all opsin channels, the

279 majority of Off- and On-responses occurred in the upper and lower part of the IPL,

280 respectively (Fig. 3d,e), in line with mammalian inner retinal circuits (Masland 2001; Wässle

281 2004; Euler et al. 2014; Franke et al. 2017). However, the transition depth between On- and

282 Off-bands differed between cone-channels, with the R-channel transitioning closer to the

283 inner nuclear layer (INL) than the other three. As a result, two achromatic bands at the top

284 (RGBU$_{Off}$, black) and in the centre (RGBU$_{On}$, white) of the IPL were separated by a layer of

285 R$_{On}$/GBU$_{Off}$ colour opponent responses (orange) (Fig. 3e). Additional R(G)$_{Off}$/BU$_{On}$ opponent

286 responses occurred at the lower edge of the IPL. The remaining response types were

287 classified as "other" and were mostly confined to the On-channel in the lower part of the IPL

288 (grey). Accordingly, in this part of the eye the inner retina was organised into distinct

289 functional layers. Moreover, as predicted from natural light, all colour opponent terminals

290 computed short- versus long-wavelength chromatic contrasts. However, this functional

291 layering was not consistently observed in other parts of the retina. In an example scan taken

292 from the strike zone, nearly all terminals exhibited strong U(B)-On responses that reached

293 far into the upper sublamina, while responses to R and G stimulation all but disappeared

294 (Fig. 3f,g) – in striking agreement with the predicted need for dedicated UV-On prey-capture

295 circuits in this part of the eye.

296

297 Together, these two examples demonstrate that the larval zebrafish IPL is functionally highly

298 anisotropic. To systematically assess how BC responses are distributed across the eye, and

299 which specific chromatic and colour opponent computations predominate, we recorded from

300 a total of n=6,568 synaptic terminals across the sagittal plane (n = 115 scans, 12 fish at 7-8

301 *dpf*), out of which n=4,099 (62%) that passed a quality criterion (SFig. 3b,c, Methods) were

302 used for further analysis. All recordings were taken in the same sagittal plane used for

303 anatomy (cf. Fig. 2f). This dataset showed that the zebrafish larval retina is functionally

304 highly anisotropic (Fig. 3h-k, cf. SFig. 3d). For example, independent of wavelength, On- and

305 Off-responses were systematically biased to the upper- and lower- visual fields, respectively.

306 Here, a disproportionate number of U$_{On}$ responses surveyed the strike zone (Fig. 3k). What

307 is the functional distribution of BCs across the larval zebrafish eye, and what do they

308 encode?

309

Large-scale functional anisotropies of the inner retina match natural spectral statistics

To assign BCs to functional clusters, we used a Mixture of Gaussian model to sort terminals independent of eye position based on their full temporo-chromatic response kernels (Fig. 4, Methods). BC terminals fell into n=26 clusters, which were further grouped into four major response groups: n=5 achromatic clusters (C_{1-5}, Fig. 4a), n=9 UV(B)-monochromatic clusters (C_{6-14}, Fig. 4b), n=6 chromatic clusters (C_{15-20}, Fig. 4c), n=5 colour opponent clusters (C_{21-25}, Fig. 4d) and n=1 discard cluster (C_X, Fig. 4e, Methods). These groups were defined based on the relative amplitudes and polarities of each cluster mean's four chromatic kernels (Methods): Equal polarity equal gain (achromatic), equal polarity different gain (chromatic and UV(B)-monochromatic) or different polarity (colour opponent). In addition, we distinguished UV(B)-monochromatic clusters from other chromatic clusters in view of the hypothesised behavioural relevance of such a channel (Fig. 1n). Their abundance and extreme short-wavelength bias indicate the existence of a dedicated UV-system that is not integrated with other chromatic retinal circuits.

For each cluster, we computed the anatomical distribution across the eye and IPL depth (right insets). This revealed that no functional BC cluster, nor any major functional group (Fig. 4f-h), was uniformly distributed across the entire field of view. Instead, most clusters predominated in either the upper or lower visual field, with some clusters in addition exhibiting a secondary bias to predominately looking forwards or outwards. In agreement with our predictions, all UV(B)-monochromatic clusters were strongly biased to the upper and forward-facing visual field (Fig. 4b,f), while all colour opponent clusters were skewed towards the lower and outwards facing visual field (Fig. 4d,g). In fact, there were effectively no colour opponent terminals that survey the world directly upwards through the nearly achromatic Snell's window. Together, all circuits potentially dealing with colour (all chromatic and opponent clusters) surveyed the lower and outward horizontal visual field, while all circuits likely to deal with achromatic computations (all UV(B)-monochromatic and

13

337 achromatic clusters) were skewed towards the upper and frontal visual field (Fig. 4h).

338 Moreover, four out of five colour opponent clusters computed short- versus long-wavelength

339 chromatic antagonisms (reminiscent of PC2 from natural scenes), while the remaining single

340 cluster (C_{23}) compared G- to all other channels (reminiscent of a mix of PCs 3 and 4) (Fig.

341 4d, cf. Fig. 1k). This set of functional anisotropies of the larval zebrafish inner retinal circuitry

342 is in strong agreement with the distribution of behaviourally meaningful chromatic content in

343 nature (Fig. 1m,n).

344

The functional layering of the larval zebrafish inner retina

346 Next, we assessed how different response types were distributed across the layers of the

347 IPL (Fig. 5). Unlike in mammals (Euler et al. 2014), BCs in most non-mammalian

348 vertebrates, including zebrafish, can have mono-, bi- and tri-stratified morphologies (Li et al.

349 2012; Connaughton & Nelson 2000). In agreement, terminals falling into individual clusters

350 were mostly distributed across 1-3 major IPL bands (Fig. 4a-e, right insets), indicating that

351 each could principally be linked to a single or small number of BC types. To establish the

352 major trends in functional organisation of the IPL, we subdivided each of the four major

353 response groups (achromatic, UV-monochromatic, chromatic, colour opponent) into their

354 "On" and "Off"-dominated response-types and assessed the distribution of each of the

355 resultant eight groups across the depth of the IPL for different positions in the eye (Fig. 5a).

356 Most response groups (Fig. 5a, rows 2-9) were largely restricted to subsets of the larval

357 zebrafish's six anatomical IPL layers (row 1, black). However, some functions were

358 distributed more broadly than others. For example, most achromatic On-terminals (row 3,

359 grey) occurred just beneath the outer ChAT band (GCL side), and could be found in any

360 eye-position – albeit at varying densities. In contrast, UV(B)-monochromatic On-terminals

361 occurred across the entire outer part of the IPL (layers 3-6) but remained near exclusively

362 restricted to the upper visual field (row 5, lilac). Other "functions" were tightly restricted in

14

363   both visual field and IPL depth. For example, colour opponent Off-dominated terminals were

364   near exclusively found in layers 1 and 3, and only in the lower visual field (row 8, brown).

365   Next, we again combined "On" and "Off" versions of each response group for clarity and

366   superimposed the resulting four histograms of the four response groups for different eye

367   positions (Fig. 5b,c). Looking up, each IPL layer contained a substantial fraction of UV(B)-

368   monochromatic terminals; only in layers 2 and 5 there were more chromatic and achromatic

369   terminals, respectively (Fig. 5b$_1$). In the strike zone, this UV(B)-dominance further intensified,

370   and shifted towards the Off-bands in the lower IPL – in line with UV-On circuits aiding the

371   detection of paramecia (Fig. 5b$_2$, cf. Fig. 1n). In contrast, there were effectively no UV-

372   monochromatic terminals looking down, and the IPL appeared more neatly divided into

373   layers differentially encoding colour opponent, chromatic and achromatic information (Fig.

374   5b$_3$). Finally, IPL circuits surveying the outward horizon had approximately balanced

375   numbers of terminals from each functional group, and a similarly neat functional organisation

376   with IPL depth as observed for the lower visual field (Fig. 5b$_4$).

377   The complexity of functional layers differed markedly, in particular between the strike zone

378   and upper visual field (Fig. 5b$_{1,2}$), compared to the lower visual field and outward horizon

379   (Fig. 5b$_{3,4}$). In the latter, the total number of peaks often used as a tell-tale for individual IPL

380   strata far exceeded the 6 traditionally used anatomical layers of the larval zebrafish IPL. This

381   suggests that this part of the eye harbours more diverse BC circuits than what is required in

382   much more "simple"-appearing circuits surveying the upper visual field.

383   A neat division of function into specific layers of the IPL for surveying the ground and

384   outward horizon, though novel in its chromatic scope and complexity, is consistent with

385   current knowledge on the functional organisation of the vertebrate inner retina (Euler et al.

386   2014; Masland 2001; Wässle 2004; Franke et al. 2017). However, the overrepresentation of

387   the UV(B)-channel in the upper and frontal visual fields, despite the presence of all other

388   cone types, is striking. Here, most visual functions appear to draw near exclusively on On-

389   and Off-UV(B)-monochromatic channels at the expense of both colour vision and the Off

15

390 achromatic channel. How does the eye build this rich functional division across visual

391 space?

392

393 **Building a functionally anisotropic retina**

394 Across all vertebrate retinas studied to date there are distinct types of BCs, each with a

395 unique anatomy, synaptic connections and functional properties (reviewed in (Euler et al.

396 2014)). Both larval and adult zebrafish have ~20 morphologically distinct BC types, with a

397 broad diversity of chromatic connections to cones in the outer retina (Li et al. 2012;

398 Connaughton & Nelson 2000; Vitorino et al. 2009), many more than the dichromatic mouse

399 (Behrens, Schubert, Haverkamp, Euler, Haverkamp, et al. 2016; Helmstaedter et al. 2013;

400 Kim et al. 2014; Greene et al. 2016; Wässle et al. 2009). Two non-mutually exclusive design

401 strategies may underlie the observed set of functional anisotropies; First, different types of

402 BCs with different functions might specifically exist only in certain parts of the retina (Zhang

403 et al. 2012; Bleckert et al. 2014). This hypothesis is, for example, supported by the absence

404 of the characteristic large terminals of On-type mixed BCs outside the ventral- and dorsal-

405 most retina (Fig. 2h,j), where rods are located (Fig. 2b,c). Second, the same types of BCs

406 may exist across the entire retina, but shifting function with position (Baden et al. 2013;

407 Joesch & Meister 2016; Chang et al. 2013; Sabbah et al. 2017).

408 We set out to test these two possibilities experimentally. For this, we used the xfz43 marker

409 line, which labels at least three morphologically well-characterised types of BCs with

410 different, known anatomical connections in the outer retina (D'Orazi et al. 2016). One Off-

411 and one On-stratifying xfz43-positive BC type each preferentially contacts R- and G-cones

412 across their large dendritic fields. Both are thus predicted to exhibit a RG-biased physiology.

413 A third, smaller On-stratifying xfz43 type indiscriminately samples from all cones, and is

414 therefore expected to encode On-achromatic features.

415   To selectively record from these cells' synaptic terminals, we crossed our *Tg(-*

416   *1.8ctbp2:SyGCaMP6)* line to *Tg(xfz43:Gal4;UAS:ntr-mCherry)* animals (Fig. 6a,b). As

417   before, this allowed recording from all BC terminals, but in addition labelled xfz43-cells are

418   simultaneously recorded in the red fluorescence channel. This dataset (64 scans, 5 fish)

419   represents a subset of the complete BC-survey presented previously (Figs. 3-5) and

420   consisted of n=620 xfz43-positive terminals, of which the 392 (63%) that passed our quality

421   criterion (Methods) fell into 2 main IPL bands (Fig. 6c, red).

422   Next, we functionally assessed xfz43 Off- and On-stratifying terminals separately. In

423   agreement with their stratification, Off- and On-stratifying terminals fell into functional Off-

424   and On-clusters, respectively (Fig. 6d,e). However, the presumed single xfz43 Off-type

425   (D'Orazi et al. 2016) fell into 6+ functional clusters that spanned all four major functional

426   groups (Fig. 6d). Similarly, the presumed two On-type xfz43 cells were sorted into 6+

427   clusters that spanned 3 major functional groups (Fig. 6e). In fact, individual examples clearly

428   demonstrated this functional diversity within a genetic type, irrespective of any clustering (not

429   shown). This extreme functional diversity of all three presumed "clean", genetically defined

430   BC types strongly suggests that - in the larval zebrafish eye - genetics alone do not predict a

431   BC's physiology. Instead, a cell's functional identity appears to fundamentally depend on its

432   surrounding neuronal network in different parts of the eye.

433   However, the allocation of xfz43-cells to functional clusters was far from random. For

434   example, xfz43 Off-terminal allocated clusters C_1, C_{15} and C_{17} all exhibited at least a small

435   RG-bias, consistent with these cells' known connectivity in the outer retina (D'Orazi et al.

436   2016). Similarly, cluster C_{18}, which captured most chromatic xfz43 On-terminals, had an RG-

437   biased physiology, while the largely achromatic cluster C_2 might reflect the cone-unselective

438   xfz43 cells. In each case, this mainly leaves several UV(B)-dominated response clusters that

439   are not explained by these cells' cone-selectivity ($C_{6-8,12,13}$).

440   Are these UV-clusters generated by UV-cone inputs with unusually high gain? For example,

441   the small On-type xfz43 cell indiscriminately integrates the outputs of fewer than 10 cones

442   (D'Orazi et al. 2016). Here, a hypothetical high-gain UV-input from only two or three cones

443   could bias a cell towards a UV-dominated response. While this hypothesis clearly needs

444   further exploration, already here several lines of evidence point at this as one mechanism of

445   functional diversification across the larval zebrafish IPL. First, under natural light, UV-cones

446   receive ~15 times fewer photons than red cones (Fig. 1h), prompting the need for a high-

447   gain amplification system for short-wavelength visual processing. In agreement, in mice the

448   gain of UV-cones appears to be higher than that of M-cones (Breuninger et al. 2011; Baden

449   et al. 2013). Second, UV-cones numerically dominate the frontal- and upper visual field (Fig.

450   2b-d). Third, UV-responses overall dominate the IPL in this part of the eye (Figs. 3k, 4b,f, 5),

451   with their kernel amplitudes often exceeding those of any other opsin channels more than

452   10-fold, despite the presence of all other cone types. Taken together, it therefore seems

453   likely that at least to some extent larval zebrafish BC types with specific function exist in only

454   parts of the eye, but that in addition more large-scale outer- and/or inner-retinal circuits can

455   "override" this genetically defined functional organisation.

456

Conclusion and outlook

458   We have shown that inner retinal circuits of larval zebrafish are exquisitely matched to their

459   natural visual environment on several levels. First, chromatic circuits are systematically

460   integrated by a neatly layered inner retina, but only at the horizon and the lower visual field,

461   which in nature contain the most chromatic information (Fig. 7a, cf. Figs. 1e,k, 4g,h, 5b).

462   Here, the chromatic computations performed by these circuits match the differential

463   predominance of different natural chromatic contrasts and behavioural demands (Fig. 4d,

464   Fig. 1k). The upper and frontal visual fields are dominated by UV-driven circuits, a

465   specialisation that begins with an anisotropic arrangement of UV-cones across the eye (Fig.

466   2b-d) and is mirrored across the ventral inner retina, apparently at the expense of circuits

467   serving colour vision and near inner retinal organisation (Fig. 7b, cf. Figs. 3k, 4f, 5). This UV-

468   dominance is likely linked to the need to spot nearby UV-bright microorganisms (Novales

18

469   Flamarique 2012) as well as the ability to detect UV-dark objects on the backdrop of further

470   UV-bright organic matter dissolved in the water (Losey et al. 1999; Nava et al. 2011;

471   Goldsmith 1994). Achromatic cone-driven circuits are used across the entire visual field, but

472   differentially use On- and Off dominant regions in the upper and lower visual field

473   respectively, possibly to drive the dorsal righting response which helps fish maintain an

474   upright posture by aligning their vertical body axis with the brightness gradient of light from

475   the sky (Fig. 7c, cf. Fig. 3h-k). Finally, rod-driven circuits exclusively survey the visual field

476   above and below the animal, likely to capitalise on the additional light caught through Snell's

477   window and its ground reflections (Fig. 7d, cf. Fig. 2b, right). To what extent this set of

478   striking regional specialisation of the larval zebrafish visual system is already established in

479   the outer retina, how it is reflected in the adult (Pita et al. 2015), and how it is used in the

480   retinal output and brain to ultimately drive behaviour will be important to address in future

481   studies.

482 **METHODS**

483

484 No statistical methods were used to predetermine sample size.

485

486 **Field sites**. Six field sites were visited in West Bengal, India (Supplementary Fig. 1) in May

487 2017, just before the monsoon season. The global positioning coordinates of each site were:

488 Site 1 (lat. 26.531390, long. 88.669265), site 2 (lat. 26.528117, long. 88.641474), site 3 (lat.

489 26.841041, long. 88.828882), site 4 (lat. 26.792305, long. 88.588003), site 5 (lat. 26.903202,

490 long. 88.554333) and site 6 (lat. 26.533690, long. 88.648729). Zebrafish of all ages were

491 found mostly in shallow pools of water adjacent to bigger streams (with exception of one

492 deeper fish farm pond, site 6), in agreement with previous work (Arunachalam et al. 2013;

493 Spence et al. 2008; Parichy 2015). The visited sites varied substantially with the type of

494 habitat (different sized streams, stagnant fish farm pond), the amount of vegetation above

495 and under water, the type of substrate and the current of the water (Supplementary Data).

496 For analysis, all recorded data was combined without prior selection.

497

498 **Hyperspectral imaging.** To gather hyperspectral images, we used a custom made, water-

499 proofed hyperspectral scanner (Nevala et al. 2017) built around a commercial spectrometer

500 (Thorlabs CCS200/M, 200-1,000 nm). In short, two spectrally broad mirrors mounted on top

501 of servo-motors were controlled by an Arduino Uno microcontroller to iteratively bring

502 different positions in visual space into the active part of the spectrometer to build up a

503 complete hyperspectral image (Baden et al. 2013). 1,000 Scan-points were spaced 1.6° and

504 defined by a Fermat's spiral, followed by a custom path-shortening algorithm. Spectra were

505 recorded using the spectrometer software OSA (Thorlabs). We used diving-weights to

506 stabilise the scanner under water. In addition, the scanner-case was placed inside a hard-

507 plastic box to maintain the upright position with a UV-transparent window pointing forward.

508   After placing the scanner to its <50 cm depth underwater position, we waited up to 5 minutes

509   for any stirred-up debris to settle. All n=31 scans were taken during the day between 11am

510   and 5pm; the weather conditions varied from slightly cloudy to clear sky, but remained

511   constant for individual measurements. Time for one scan acquisition varied between 4 and 8

512   minutes, depending on the set mirror-move times (200-500 ms) and integration times (80-

513   200 ms) which were adjusted for each measurement to yield an approximately consistent

514   signal-to-noise independent of absolute light intensity in each scene. Finally, in each case in

515   addition to the scan a 180° still image was taken approximately at the scanner position with

516   an action camera (Campark ACT80 3K 360°). Stills were mapped to the 2D plane by a

517   standard angular fisheye projection to 720x720 pixels (0.25° per pixel).

518

519   **Animals and tissue preparation.** All procedures were performed in accordance with the UK

520   Animals (Scientific Procedures) act 1986 and approved by the animal welfare committee of

521   the University of Sussex. For all experiments, we used 7-8 days post fertilisation (*dpf*)

522   zebrafish (*Danio rerio*) larvae of either sex. The following transgenic lines were used: *Tg(-*

523   *1.8ctbp2:SyGCaMP6)*, *Tg(xfz43:Gal4;UAS:ntr-mCherry;-1.8ctbp2:SyGCaMP6)* (Zhao et al.

524   2009), *Tg(opn1sw1:GFP)* (Takechi et al. 2003), *Tg(-3.2opn1sw2:mCherry)* (Salbreux et al.

525   2012), *Tg(thrb:Tomato)* (Suzuki et al. 2013). In addition, a *Tg(xops:ntr-mCherry)* line was

526   generated by injecting pXops-nfsB-mCherry plasmid into one-cell stage eggs and

527   subsequently screening for the expression of mCherry among progenies of injected fish.

528   pXops-nfsB-mCherry plasmid was constructed by replacing EGFP with nfsB-mCherry in

529   XopsEGFP-N1 plasmid (Fadool 2003).

530   Owing to the exploratory nature of our study, we did not use randomisation and blinding.

531   Animals were housed under a standard 14:10 day/night rhythm and fed 3 times a day.

532   Animals were grown in 200 µM 1-phenyl-2-thiourea (Sigma) from 1 *dpf* to prevent

533   melanogenesis (Karlsson et al. 2001). For 2-photon *in-vivo* imaging, zebrafish larvae were

534   immobilised in 2% low melting point agarose (Fisher Scientific, Cat: BP1360-100), placed on

535   the side on a glass coverslip and submersed in fish water. Eye movements were further

536   prevented by injection of α-bungarotoxin (1 nl of 2 mg/ml; Tocris, Cat: 2133) into the ocular

537   muscles behind the eye. For immunohistochemistry, larvae were culled by tricaine overdose

538   (800 mg/l) at 7-8 *dpf*. Whole larvae were fixed in 4% paraformaldehyde for 25 min before

539   being washed in phosphate-buffered saline (PBS).

540

541   **Two-photon Ca^{2+} imaging and light stimulation.** We used a MOM-type two-photon

542   microscope (designed by W. Denk, MPI, Martinsried; purchased through Sutter

543   Instruments/Science Products). Design and procedures were described previously (Euler et

544   al. 2009). In brief, the system was equipped with a mode-locked Ti:Sapphire laser

545   (Chameleon Vision-S, Coherent) tuned to 927 nm, two fluorescence detection channels for

546   GCaMP6f (F48x573, AHF/Chroma) and mCherry (F39x628, AHF/Chroma), and a water

547   immersion objective (W Plan-Apochromat 20x/1,0 DIC M27, Zeiss). For imaging mCherry,

548   we used 960 nm excitation instead. For image acquisition, we used custom-written software

549   (ScanM, by M. Mueller, MPI, Martinsried and T. Euler, CIN, Tuebingen) running under IGOR

550   pro 6.3 for Windows (Wavemetrics), taking 64 x 32 pixel image sequences (15.625 frames

551   per s) for activity scans or 512 x 512 pixel images for high-resolution morphology scans.

552   For light stimulation, we focussed a custom-built stimulator through the objective, fitted with

553   band-pass-filtered light-emitting diodes (LEDs) ('red' 588 nm, B5B-434-TY, 13.5cd, 8°, 20

554   mA; 'green' 477 nm, RLS-5B475-S; 3-4 cd, 15°, 20mA; 'blue' 415 nm, VL415-5-15; 10-16

555   mW, 15°, 20 mA; 'ultraviolet, UV' 365 nm, LED365-06Z; 5.5 mW, 4°, 20 mA, Roithner,

556   Germany). LEDs were filtered and combined using FF01-370/36, T450/pxr, ET420/40m,

557   T400LP, ET480/40x, H560LPXR (AHF/Chroma). The final spectra approximated the peak

558   spectral sensitivity of zebrafish R-, G-, B-, and UV-opsins, respectively, while avoiding the

559   microscope's two detection bands (SFig. 3a). LEDs were synchronised with the scan retrace

560   at 500 Hz. Stimulator intensity was calibrated (in photons per second per cone) such that

561   each LED would stimulate its respective zebrafish cone-type with an equal number of

562   photons (~10^5 photons per cone per s). Assuming an effective absorption coefficient of ~0.1,

563   this translates to ~10^4 photoisomerisations per cone per s (R*), a low photopic regime. We

564   did not attempt to compensate for cross-activation of other cones, and relative LED-versus-

565   opsin cross sections are listed in SFig. 3a. Owing to two-photon excitation of photopigments,

566   an additional, steady illumination of ~10^4 R* was present during the recordings (for detailed

567   discussion, see (Baden et al. 2013; Euler et al. 2009)). For all experiments, the animal was

568   kept at constant illumination for at least 5 seconds after the laser scanning started before

569   light stimuli were presented. The only stimulus used throughout this work was a

570   "tetrachromatic binary noise" stimulus. Here, each of the 4 LEDs was simultaneously but

571   independently driven in a known binary sequence at 12.8 Hz for 258 seconds.

572

573   **Immunohistochemistry.** For the IPL structural analysis, whole fixed larvae (7-8 *dpf*) were

574   incubated in permeabilisation/blocking buffer (PBS with 0.5% Triton-X 100 and 5% normal

575   donkey serum) for at least 10 min followed by 3-5 days incubation at 4°C with primary

576   antibodies (chicken anti-GFP (AbCam, 13970, 1:500), goat anti-ChAT (Chemicon, AB144P,

577   1:50), rabbit anti-PKCα (Sigma, P4334, 1:100)). Samples were rinsed three times in

578   phosphate buffered saline with 0.5% Trion-X 100 and incubated for another day with

579   secondary antibodies and Hoechst 33342 (1:5000) for nucleus staining in

580   permeabilisation/blocking buffer. Finally, samples were washed in PBS with 0.5% Triton-X

581   100 and mounted in mounting media (VectaShield, Vector, H-1000) for fluorescent imaging.

582   Secondary antibodies used were as follows: Donkey anti-chicken IgG CF488A conjugate

583   (Sigma, 1:500), Donkey anti-rabbit IgG CF568 conjugate (Sigma, 1:500), Donkey anti-goat

584   IgG DyLight650 conjugate (BETHYL, 1:200). For photoreceptors, whole eyes were dissected

585   from the animal at 7-8 *dpf* and subsequent tissues were subjected to immunohistochemistry

586   as described above. Antibodies used are, a primary antibody: zpr-1 (ZFIN, 1:50), and a

587   secondary antibody: Donkey anti-mouse IgG DyLight649 conjugate (Jackson

588   Immunoresearch laboratories, 1:500). Confocal images were taken on Leica TCS SP8 or

23

589   Olympus FV1000 using objectives 63x (HC PL APO oil CS2, Leica), 20x (HC PL APO Dry

590   CS2, Leica), 60x (UPLSAPO oil, Olympus) or 20x (UPLSAPO oil, Olympus) at xy: 0.1-0.07

591   µm/pixel, and z-step: 0.25-0.3 µm for high-resolution images and 0.7-0.5 µm/pixel, and z-

592   step: 2 µm for low magnification images. Images were median-filtered and contrast and

593   brightness were adjusted in Fiji (NIH).

594

595   **Photoreceptor densities.** Confocal image stacks of whole eyes were converted to spherical

596   max-projection image stacks using custom-written scripts in IGOR pro 6.3 (Wavemetrics).

597   The image plane crossing photoreceptor somata in this spherical projection was used to

598   automatically identify cells using a threshold function in SARFIA (Dorostkar et al. 2010)

599   running under IGOR Pro. After manual verification and correction in Fiji, photoreceptor

600   positions were projected back onto a 3D hemi-sphere and density was calculated using

601   custom IGOR Pro scripts. Density maps (Fig. 2a,b) are top-down views of these 3D hemi-

602   spheres. For extracting density profiles linearlised against eye position (Figs. 2c,d) we

603   computed the mean density in a ring between 112°-145° eccentricity, whose angular centre

604   of mass corresponds to 130°. This "3D ring" was chosen as it corresponds to the same

605   sagittal plane as surveyed for inner retinal anatomy and function (Fig. 2e, SFig. 2).

606

607   **Data analysis.** Data analysis was performed using IGOR Pro 6.3 (Wavemetrics), Fiji (NIH)

608   and Python 3.5 (Anaconda distribution, scikit-learn 0.18.1, scipy 0.19.0 and pandas 0.20.1).

609

610   **Pre-processing and receptive field mapping.** Regions of interest (ROIs), corresponding to

611   individual presynaptic terminals of BCs were defined semi-automatically by custom software

612   (D. Velychko, cf. (Baden et al. 2016)). Next, the Ca^{2+} traces for each ROI were extracted and

613   de-trended by high-pass filtering above ~0.1 Hz and followed by z-normalisation based on

614   the time interval 1-6 seconds at the beginning of recordings using custom-written routines

24

615   under IGOR Pro. A stimulus time marker embedded in the recording data served to align the

616   Ca^{2+} traces relative to the visual stimulus with a temporal precision of 2 ms. We then

617   mapped linear receptive fields of each ROI by computing the Ca^{2+} transient-triggered-

618   average. To this end, we resampled the time-derivative of each trace to match the stimulus-

619   alignment rate of 500 Hz and used thresholding above 0.7 standard deviations relative to the

620   baseline noise to the times t_i at which Calcium transients occurred. We then computed the

621   Ca^{2+} transient-triggered average stimulus, weighting each sample by the steepness of the

622   transient:

623    $$F(l,\tau) = \frac{1}{M}\sum_{i=1}^{M} \dot{c}(t_i)S(o, t_i + \tau)$$

624

625   Here, $S(l,t)$ is the stimulus ("LED" and "time"), τ is the time lag (ranging from approx. -1,000

626   to 350 ms) and M is the number of Ca^{2+} events. RFs are shown in z-scores for each LED,

627   normalised to the first 50 ms of the time-lag. To select ROIs with a non-random temporal

628   kernel, we first concatenated all four colour kernels to a single vector (X by 1) and computed

629   the standard deviation across this vector. We used all ROIs with a standard deviation of at

630   least two. The precise choice of this quality criterion does not have a major effect on the

631   results.

632

633   **Feature extraction and Clustering.** For each ROI, we concatenated the kernels for all

634   colours, forming one 2,496-dimensional vector (4 times 649) per ROI. We then denoised this

635   vector by using the reconstruction obtained from projecting it on the first 40 PCA

636   components, capturing ~90% of the variance. We then followed a feature extraction and

637   clustering pipeline described previously (Baden et al. 2016). We computed three PCA

638   features on each colour channel individually, yielding a total of 12 features. They captured

639   between 70 and 83% of the variance per channel. We fit a Gaussian Mixture Model the data,

640   optimizing the Bayesian Information Criterion (BIC) for the number of mixture components.

641 The covariance matrix of each cluster was chosen to be diagonal and a regularisation term

642 of 10^{-6} was added to the diagonal. The BIC curve was shallow between 22 and 27 clusters,

643 with a minimum at 26. Spherical covariance matrices or the same covariance matrix for each

644 cluster yielded higher BIC scores. Full covariance matrices yielded somewhat lower BIC

645 scores with an optimum at a cluster number below 10. In this case, functionally

646 heterogenous clusters were grouped together. This analysis was performed in Python 3.5

647 using scikit-learn implementations.

648

649 **Grouping of clusters into response groups.** Each cluster was allocated into one of four

650 response groups (n=25) or discarded (n=1). For each cluster mean and each channel, we

651 first calculated the peak to peak amplitude in z-scores relative to each channels baseline,

652 defined as the first 50 ms of each kernel. If the mean difference of the mode of all amplitudes

653 between the UV and all other channels exceeded 35, that cluster was classified as UV(B)

654 monochromatic (C_{6-14}). Similarly, a single cluster with mean mode amplitude below 2 was

655 discarded (C_x). Next, we calculated the correlation between all pairs of channels as well as

656 the variance between amplitudes, with the mean between amplitudes normalised to 1. If the

657 mean correlation between all pairs exceeded 0.8 (i.e. similar waveforms) and the variance of

658 amplitudes was below 0.09 (i.e. similar amplitudes), that cluster was classified as achromatic

659 (C_{1-5}). Finally, to distinguish remaining chromatic (C_{15-20}) and colour opponent clusters (C_{21-25}), we also computed the mean of the mode of all correlations. If the mean of correlation

660 equalled the mean of the mode of correlations (i.e. all kernels had the same polarity), that

661 cluster was classified as chromatic. All remaining clusters were classified as colour

662 opponent. Following this automatic pre-sorting, we manually reallocated three clusters that

663 were misclassified due to low amplitudes of individual kernels: C_{17} and C_{20} were moved from

665 colour opponent to chromatic as the very low amplitudes of the R-channel led to these

666 clusters' erroneous classification, and C_9 was moved from the chromatic to the UV(B)

667 monochromatic group as this cluster effectively only responded to UV-stimulation but the

26

668   overall low-amplitudes led its misclassification. Finally, we also moved C_{21} from the

669   chromatic to the opponent group. Here, the pronounced time-course difference between

670   UV(B) and RG that leads to a clear opponency in the early kernel period was not picked up

671   by our automatic sorting rules.

672

673   **Histograms against eye position.** All histograms against eye position were smoothed

674   using a circular 60° binomial (Gaussian) filter along the x-dimension and IPL depth

675   histograms were in addition smoothed by a 5%-width Gaussian filter across the y-dimension.

676   Moreover, all 2D histograms of both eye position and IPL depth (Figures 4-6) were warped

677   to horizontally align the peaks of the major anatomical IPL layers across eye position (Fig.

678   5a, top row). Specifically, the IPL was compressed from the top by 5% at the outwards

679   horizon and by 5% from the bottom of the IPL at the forward horizon, where the IPL is

680   thickest (cf. Fig. 2k).

681

FIGURE LEGENDS

Figure 1 | Distribution of chromatic content in the zebrafish natural visual world. a, Example 180° underwater photograph taken in zebrafish-inhabited waters in West Bengal, India and **b-d,** the first three principal components across the chromatic dimension (R,G,B) of the image in (a). PC1 reflects the achromatic image content, while PCs 2 and 3 (false-colour coded in shades of yellow) reflect the remaining chromatic content. **e,** Variance explained by PC3 and PC2+3 across all 31 images calculated from 5° horizontal images slices. Error-shadings in s.d.. **f,** Schematic of the custom-built hyperspectral scanner. X and Y mirrors are moved through 1000 regularly spaced positions over a 60° circular window to deflect a ~2.8° spot of light into a spectrometer and thereby build up a hyperspectral image (Baden et al. 2013; Nevala et al. 2017). **g,** Mean of n=31,000 peak-normalised underwater spectra (31 horizon-aligned scenes of 1000 pixels each) and mean spectrum of the sky in zenith above the water. Shading in s.d.. **h,** Zebrafish opsin complement (UV: U, Blue: B, Green: G, red: R), which each opsin-template multiplied with the mean underwater spectrum from (g) to estimate relative photon-catch rates in nature. Templates based on (Baden et al. 2013), for discussion on spectral positions see Supplementary Materials. **i,** Enlargement and **j,** reconstruction of photographed scene (a) from scanner-data by multiplying each pixel's spectrum with each opsin template (h). Scan-reconstructions are truncated beyond 20° from the centre to remove sampling edge artefacts. **k,** Mean loadings of PCs 1-4 across all n=31 scans. **l,** As (e), cumulative variance explained by PCs 2-4 calculated separately for 5° vertical slices across all n=31 scanned scenes. Error-shadings in s.d.. As before (e), most chromatic information exists at and below the horizon. **m,** Schematic summary of natural chromatic statistics and **n,** of expected behaviourally important short-wavelength specific visual requirements. Larval schematic modified from L. Griffiths.

Figure 2 | Anisotropic retinal structure. a, 3D confocal stack taken across the entire retina of an 8 *dpf* larva (*Tg(Opn1sw1:GFP)*) with all UV-cones fluorescently labelled was used for

28

709 semi-automated quantification of cone densities across the retina (Methods). **b**, Average

710 densities of all four cone types and rods across the retina, based on n=6 (R), 6 (G), 5 (B), 5

711 (U), 4 (rods) retinas (*Tg(thrb:Tomato)* for R, zpr-1 antibody staining for G, *Tg(-*

712 *3.5opn1sw2:mCherry)* for B, *Tg(opn1sw1:GFP)* for U, and *Tg(xops:ntr-mCherry)* for rod).

713 Colour Scales: 0 (white) – 35,000 (black) cones mm^{-2} or 0-9,000 rods mm^{-2}. D, Dorsal, T,

714 Temporal, V, Ventral. N, Nasal. **c-e,** To compare cone distributions across retinal positions

715 (c,d), we computed densities at sagittal plane approximately aligned with the back-surface of

716 the lens (e, Methods). This plane projects in a ~130° cone from the eye centre, with eyes

717 rotated ~36.5° forward during prey capture (18.5° at rest, SFig. 2a,b). Cone and rod

718 densities across the plane defined in (e) on a linear scale of the fish's egocentric visual field.

719 Dashed lines indicate the forward and outward horizon. (d) is as (c), plotted in polar

720 coordinates relative to the body of the fish as indicated. **f,** Whole-eye immunostaining of an 8

721 *dpf Tg(-1.8ctbp2:SyGCaMP6)* larvae labelled against green-fluorescent protein (GFP,

722 bipolar cell (BC) terminals, green), choline acetyltransferase (ChAT, cholinergic amacrine

723 cells, cyan) and protein kinase C alpha (PKCα, On-BCs, magenta). Shown is the same

724 sagittal section used in (f-h). Scalebar 50 µm. OPL, outer plexiform layer; INL, inner nuclear

725 layer; IPL, inner plexiform layer; GCL, ganglion cell layer. **g-j,** Higher magnification sections

726 from (f) showing the IPL at different positions across the eye as indicated. For clarity,

727 GFP/PKCα (g$_1$-j$_1$) and ChAT/PKCα (g$_2$-j$_2$) are shown separately. Scalebar 5 µm. **k,** Mean IPL

728 thickness across n=5 whole-eye immunostainings as in (f) and **l,** mean signal in the three

729 fluorescence channels as above.

730

731 **Figure 3 | Surveying inner retinal chromatic responses *in vivo*. a,** 2-photon scan-field

732 (32 x 64 pixels, 15.625 Hz) of a nasal IPL section (outward horizon) in a *Tg(-*

733 *1.8ctbp2:SyGCaMP6)* larvae for simultaneous recording of light-driven calcium responses

734 across the entire IPL depth at single terminal resolution (top) and regions of interest (ROIs,

735 bottom). Scalebar 5 µm. **b,** example of calcium responses to tetrachromatic binary white

736 noise stimulation (12.8 Hz, Methods) of two ROIs highlighted in (a). **c,** tetrachromatic linear

737 filters ("kernels") recovered by reverse correlation of each ROI's response with the noise

738 stimulus (b). The colour code indicates the stimulus channel (R, G, B, U cf. SFig. 3a). **d,** For

739 each stimulus channel, we classified each ROI's kernel as either "On" (in red, green, blue or

740 purple), "Off" (black), or non-responding (no marker) and plotted each response over the

741 anatomical scan image (Methods). **e,** By comparison across the four stimulus channels, we

742 then classified each ROI as either achromatic "Off" (R+G+B+U Off, black) or "On"

743 (R+G+B+U On, white), Colour opponent (any opposite polarity responses in a single ROI,

744 orange) or "other" (grey) and again plotted each ROI across the IPL to reveal clear chromatic

745 and achromatic layering in this scan. **f,g,** As (d,e), but for a scan taken in the temporo-

746 ventral retina which surveys the world in front of the animal just above the visual horizon.

747 This zone is critical for prey capture, and was thus dubbed "strike zone". **h-k,** Distribution of

748 all On- and Off-responses per stimulus channel (h, red; i, green; j, blue; k, UV) based on n =

749 4,099 / 6,565 ROIs that passed a minimum quality criterion (Methods) sampled from across

750 the entire sagittal plane (115 scans, 12 fish).

751

752 **Figure 4 | The functional organisation of the larval zebrafish eye**. Mixture of Gaussian

753 clustering of all n=4,099 responding terminals based on the full waveforms of their

754 tetrachromatic kernels, with cluster number limited by the Bayesian Information Criterion

755 (BIC), yielded 25 clusters (C_{1-25}) and 1 discard cluster (C_X). For simplicity, each cluster was

756 further allocated to one of four major response groups (Methods): **a,** achromatic (C_{1-5}), **b,**

757 UV(B)-monochromatic (C_{6-14}), **c,** chromatic (C_{15-20}) and **d,** colour opponent (C_{21-25}). **e,**

758 Discard cluster C_x. For each cluster, shown are the time-course of each kernel (left

759 heatmaps, lighter shades indicating higher values), the cluster-means (middle) and their

760 anatomical distribution across IPL depth (y axis) and position in the eye (x-axis, right

761 heatmaps, lighter shades indicate higher abundance). Dashed lines indicate the forward and

762 outwards horizon, the asterisk denotes the position of the strike zone. The height of each

30

763   cluster's left heatmap indicates its number of allocated terminals. **f-h,** Linear (left) and polar

764   (right) histograms of terminal abundance of the functional groups defined in (a-e) across the

765   larval zebrafish's visual space. **f,** UV(B)-monochromatic (purple) and achromatic (grey)

766   groups, **g,** chromatic (yellow) and colour opponent (orange) groups, **h,** summed UV(B)-

767   monochromatic and achromatic groups (grey) versus chromatic and colour opponent groups

768   (brown).

769

770   **Figure 5 | Distribution of function across the IPL. a,** Histograms of terminal abundance

771   across IPL depth (y axis) and position in the eye (set of histograms) for each functional

772   group (cf. Fig. 7), divided by On- and Off-dominated responses as indicated. In addition, the

773   distribution of all n = 6,565 scanned terminals independent of response-quality is plotted to

774   reveal the anatomical distribution of all BC terminals (top, light grey). Heatmaps to the right

775   show the same data in a single image. Asterisk denotes the position of the strike zone.

776   Dashed lines indicate the forward and outward visual horizon. Solid horizontal lines indicate

777   the position of the lower ChAT band as an anatomical reference. **b$_{1-4}$,** On/Off-collapsed

778   histograms of the four response groups for four example regions (up: ventral, strike zone:

779   temporo-ventral, down: dorsal and outward horizon: nasal as indicated) summarise the

780   functional IPL layering across eye positions, with approximate anatomical layers indicated in

781   the background shading. For clarity, achromatic and UV(B)-monochromatic histograms are

782   x-axis-reversed. **c,** Colour-coded response groups (top) plotted against eye position (x) and

783   IPL depth (y) and merge (bottom). Throughout, colours indicate the functional groups:

784   Achromatic (grey/black), UV(B)-monochromatic (purple/violet), chromatic (yellow/beige) and

785   colour opponent (orange/brown).

786

787   **Figure 6 | Distribution of genetically defined BC-types. a,** High-resolution 2-photon scan

788   of a ventro-nasal (up/outward) IPL section in 7 *dpf* larvae expressing SyGCaMP6f under

789   *ctbp2* promoter (green) as well as mCherry under *xfz43* (red). Scalebar 5 µm. **b,** Subsequent

790   higher rate scans during light-stimulation allowed recovering tetrachromatic kernels from

791   individual xfz43-positive terminals as before (right). **c,** Distribution of 392 / 620 xfz43-positive

792   BC terminals (64 scans, 5 fish) that passed our response criterion (red, Methods) across the

793   IPL (y) and eye (x), superimposed on the distribution of all terminals from the same scans

794   (green). The heatmap on the right shows only xfz43 positive terminals. Dashed lines indicate

795   the forward and outward horizon, while the solid horizontal line indicates the position of the

796   lower ChAT band. **d,** Allocation of all xfz43-positive anatomical Off terminals to functional

797   clusters (right) and distribution of these terminals across the eye by functional group (left). **e,**

798   As (d), but for xfz43-positive anatomical On-cells.

799

800   **Figure 7 | The larval zebrafish eye's chromatic organisation for vision in nature. a,**

801   Circuits for colour vision are generally biased to the horizon and lower visual field where

802   most chromatic content is found in nature. **b,** Circuits for UV(B)-monochromatic vision

803   dominate the upper and frontal visual field and may be used for prey-capture and the

804   detection of UV-dark silhouettes against a UV-bright background. **c,** Achromatic circuits are

805   found throughout the eye, with On- and Off- circuits dominating the upper-frontal and lower-

806   outward facing visual fields, respectively. **d,** Rod-circuits are exclusively used to survey the

807   sky directly above and the ground reflection directly beneath the animal, where most

808   photons can be caught. In each image, the triangular area above the animal depicts Snell's

809   window, and the visual horizon is indicated by a dashed line.

810

811 **SUPPLEMENTARY MATERIALS**

812

813 **The cone-opsin complement of zebrafish.** While larval (and adult) zebrafish have four

814 cone-types and one rod-type, each cone's *in vivo* action spectrum depends on several

815 factors, including which opsin gene(s) are expressed, which retinal chromophore(s) are

816 used, and what fraction of the spectrum of light is filtered out by the optical apparatus. To

817 justify the choice of opsin templates used (cf. SFig. 3a) we will discuss each in turn.

818 Zebrafish have UV, blue, green and red sensitive cones in their retina. The maximal

819 absorbance (λ_{max}) for the UV sensitive cones (UVS) lies around 360-365 nm while the λ_{max}

820 for the blue sensitive cones (SWS, short wavelength sensitive cone) is at 411nm (Allison et

821 al. 2004; Hunt et al. 2001). For green and red cones (medium and long wavelength sensitive

822 cones, MWS and LWS) the situation is more complex since these cones can express

823 different types of opsins. Zebrafish use four MWS-cone opsins (RH2-1, RH2-2, RH2-3 and

824 RH2-4) and two LWS-cone opsins (LWS1 and LWS2) (Chinen et al. 2003). All these opsins

825 have different spectral sensitivities, and all are expressed in the retina (Takechi & Kawamura

826 2005). This variation is expected in a small spectral sensitivity shift in these cones with

827 retinal position. Based on the abundance of the opsin type across the retina for the green

828 and red cones during the early development of zebrafish larvae, we chose the most

829 abundant opsin type in each case: the RH2-1 gene (λ_{max} at 467 nm) for the green cones and

830 the LWS1 gene (λ_{max} at 548 nm) for the red cones.

831 In addition, vertebrates can use two different chromophores: 11-cis-retinal (vitamin A1) and

832 11-cis-3,4-didehydroretinal (vitamin A2). The A2 chromophore holds one extra double bond

833 compared to A1, which lowers the energy needed to initiate the phototransduction cascade

834 (Enright et al. 2015; Koskelainen et al. 2000; Loew & Dartnall 1976). By changing the

835 chromophore from A1 to A2, a visual pigment's peak spectral sensitivity can be shifted to

836 longer wavelengths. While for UVS- and SWS-opsins, this switch has little effect, MWS-

33

837   opsins can be shifted by 20 nm, while LWS-opsins shift up to 60 nm (Allison et al., 2004).

838   This change can be triggered in adult zebrafish when treated with thyroid hormone (Allison

839   et al., 2004; Enright et al., 2015), but there is no clear evidence for the zebrafish of any age

840   holding the A2 chromophore under normal conditions. We therefore assumed that only the

841   A1 chromophore is present. As such, λ_{max} values for the cone templates were set to 365 nm,

842   411 nm, 467 nm and 548 nm for the four cone types, respectively.

843   Other possible structures in the eye filtering the light reaching the light sensitive cells are the

844   cornea, the lens and the vitreous body. All these parts can hold patches of pigments that

845   mostly absorb shorter wavelengths (UV) affecting the spectrum of light that eventually

846   reaches the photoreceptors (Douglas & McGuigan 1989). Whether or not the animal has

847   these pigments varies widely across different species (Siebeck & Marshall 2001), but

848   measurements are still lacking for the larval zebrafish. Notably, here the small size of the

849   eye, and the fact that UV-cones exist throughout the retina, strongly suggest that UV-filtering

850   by the optical apparatus in these animals is negligible. As such, we did not correct our opsin

851   templates for any putative spectral related to the optical apparatus of the eye.

852

853   **The number of neurons in the 7-8 *dpf* larval zebrafish.** Our photoreceptor-labelling

854   experiments (Fig. 2) revealed that at 7-8 *dpf*, a single eye comprises approximately 10,000

855   photoreceptors (all cones and rods combined). From here, we then estimated HC and BC

856   numbers as ~1,000 and ~25,000, assuming these neuron classes comprise 4 (HC) and 25

857   (BC) types that each tile the retina with no overlap, with each type on average contacting 30

858   (HC) and 10 (BC) PRs (D'Orazi et al. 2016; Li et al. 2009; Vitorino et al. 2009; Song et al.

859   2008). Finally, there are ~4,000 RGCs in the larval zebrafish eye (Robles et al. 2014), and

860   from here we assumed that ACs make up at least another 4,000 neurons. This puts the total

861   number of neurons for both eye added up ~88,000. In comparison to ~85,000-100,000

862   neurons in the brain excluding the eyes (Naumann et al. 2010), this estimate implies that

863   about half the brain's neurons are located in the eyes.

864 **Choice of age of zebrafish larvae.** Throughout this work we used 7-8 *dpf* zebrafish larvae

865 of either sex. At this age, zebrafish brain and retina conform to the anatomical structures of

866 vertebrate nervous system, such as existence of canonical cell types and specific neural

867 circuits (McLean & Fetcho 2011; Hoon et al. 2014). Supported by their visual circuits, 7-8 *dpf*

868 zebrafish larvae perform a wide range of behaviours including reflexive responses as well as

869 prey-capture and predator avoidance (Orger 2016; Friedrich et al. 2010), allowing them to

870 feed independently, navigate their environment and avoid predators. Though under constant

871 development, larval zebrafish of this age are therefore fully autonomous and highly visual

872 animals. They have been used extensively to study vertebrate nervous system organisation

873 and function including benchmark studies of whole-brain functional imaging (Keller et al.

874 2014) and serial-section electron microscopy (Hildebrand et al. 2017).

875

876 **SUPPLEMENTARY FIGURE LEGENDS**

877 **Supplementary Figure 1 | related to Figure 1: Distribution of chromatic content in the**

878 **zebrafish natural visual world. a,** Location of field sites visited in West Bengal, India. **b**,

879 Mean of n=31 action camera images and **c**, mean z-normalised brightness of the red, green

880 and blue camera channels across these scenes. **d**, As (c), with mean between all 3 channels

881 subtracted to highlight the differences between the three channels. Errors in c,d in s.e.m. **e**,

882 Principal components 1-4 (left to right) of the hyperspectral example image shown in Fig. 1j,

883 (cf. Fig. 1b-d). **f**, Achromatic-mean-subtracted mean luminance of the 4 opsin channels from

884 the same scene (like in d). Errors in s.e.m..

885

886 **Supplementary Figure 2 | related to Figure 2: Anisotropic retinal structure. a,**

887 Transverse plane (looking down onto the fish from the top) immunolabelled 7 *dpf* larval

888 zebrafish eye with bipolar cell terminals in green (like Fig. 2i) highlights the ~130° visual

889 angle surveyed by the sagittal plane used throughout this work (indicated in red). **b**, 3D

890 illustrations of the field of view covered by this sagittal plane during "rest" (eyes tilted forward

891 ~18.5°) and during prey-capture ("hunting", eyes at 35.5°) as indicated. In the top left panel,

892 the ~163° full field of view of the eye is indicated in addition to the 130° field surveyed in this

893 work.

894

895 **Supplementary Figure 3 | related to Figure 3: Surveying inner retinal chromatic**

896 **responses *in vivo*. a,** Cone action spectra (thin lines) plotted on top of effective LED

897 spectra as measured at the sample plane (black lines) and each LED's spectral cross-

898 section with respective target cone in solid colours. Grey boxes indicate the positions of the

899 two detector bands. Cross activation efficiencies between LEDs and each cone action

900 spectrum are listed in the inset. **b**, Histogram of quality criterion (Methods) for all recorded

901 terminals with cut-off value of 2 z-scores indicated and **c**, distribution of all (light) and

902   selected (dark) terminals across the eye.   **d**, Distribution of R, G, B, U Off- and On-

903   responses across the IPL depth (vertical axis) and eye position (horizontal axis) as indicated

904   (cf. Figs. 3h-k). The insets to the right show the same data plotted as heatmaps.

905

906   **Supplementary Figure 4 | related to Figure 6: Distribution of genetically defined BC-**

907   **types. a,** Distribution of xfz43-positive BC responses split by polarity (Off / On) and allocated

908   major response group plotted against IPL depth (vertical axis) and eye position (horizontal

909   axis).   **b**,   Same   data   as   (a),   plotted   as   heatmaps.

910 **Author contributions**

911 MJYZ, NEN, TY and TB designed the study, with help from DEN, DO and PB; MJYZ and TY

912 performed 2-photon imaging experiments and immunohistochemistry; TY generated all novel

913 zebrafish lines; NEN and TB built the hyperspectral scanner and performed field work; NEN,

914 MJYZ and TY performed pre-processing with inputs from TB; PB developed the clustering

915 framework; TB analysed the data with help from all authors; TB wrote the manuscript with

916 help from PB and inputs from all authors.

917

918 **Acknowledgements**

931

REFERENCES

Allison, W.T. et al., 2004. Visual pigment composition in zebrafish: Evidence for a rhodopsin–porphyropsin interchange system. *Visual Neuroscience*, 21(6):945–52.

Arunachalam, M. et al., 2013. Natural history of zebrafish (Danio rerio) in India. *Zebrafish*, 10(1):1–14.

Attneave, F., 1954. Some informational aspects of visual perception. *Psychological review*, 61(3):183–93.

Avdesh, A. et al., 2010. Natural Colour Preference in the Zebrafish (Danio rerio). *Proceedings of Measuring Behaviour*, 155–57.

Baden, T. et al., 2013. A tale of two retinal domains: near-optimal sampling of achromatic contrasts in natural scenes through asymmetric photoreceptor distribution. *Neuron*, 80(5):1206–17.

Baden, T. et al., 2016. The functional diversity of retinal ganglion cells in the mouse. *Nature*, 529(7586):345–50.

Barlow, H.B.H., 1961. Possible principles underlying the transformation of sensory messages. In *Sensory Communication*. 217–34.

Behrens, C., Schubert, T., Haverkamp, S., Euler, T., Berens, P., et al., 2016. Connectivity map of bipolar cells and photoreceptors in the mouse retina. *eLife*, 5:1206–17.

Bianco, I.H., Kampff, A.R. & Engert, F., 2011. Prey Capture Behavior Evoked by Simple Visual Stimuli in Larval Zebrafish. *Frontiers in Systems Neuroscience*, 5:101.

Bleckert, A. et al., 2014. Visual space is represented by nonmatching topographies of distinct mouse retinal ganglion cell types. *Current Biology,* 24(3):310–5.

Breuninger, T. et al., 2011. Chromatic bipolar cell pathways in the mouse retina. *The Journal of Neuroscience*, 31(17): 6504–17.

956   Buchsbaum, G. & Gottschalk, A, 1983. Trichromacy, opponent colours coding and optimum

957   colour information transmission in the retina. *Proceedings of the Royal Society of*

958   *London B,* 220(1218):89–113.

959   Calderone, J.B. & Jacobs, G.H., 1995. Regional variations in the relative sensitivity to UV

960   light in the mouse retina. *Visual Neuroscience*, 12(3):463–68.

961   Chang, L., Breuninger, T. & Euler, T., 2013. Chromatic coding from cone-type unselective

962   circuits in the mouse retina. *Neuron*, 77(3):559–71.

963   Chiao, C.C., Cronin, T.W. & Osorio, D., 2000. Color signals in natural scenes: characteristics

964   of reflectance spectra and effects of natural illuminants. *Journal of the Optical Society*

965   *of America. A,* 17(2):218–24.

966   Chichilnisky, E.J., 2001. A simple white noise analysis of neuronal light. Network

967   Computation in Neural Systems, 12(2):199–213.

968   Chinen, A. et al., 2003. Gene duplication and spectral diversification of cone visual pigments

969   of zebrafish. *Genetics*, 163(2):663–675.

970   Connaughton, V.P. & Nelson, R., 2000. Axonal stratification patterns and glutamate-gated

971   conductance mechanisms in zebrafish retinal bipolar cells. *The Journal of Physiology*,

972   524:135–46.

973   Cronin, T.W. et al., 2014. *Visual Ecology* 1st ed., Princeton University Press.

974   Cronin, T.W. & Bok, M.J., 2016. Photoreception and vision in the ultraviolet. *The Journal of*

975   *Experimental Biology*, 219(18):2790–801.

976   D'Orazi, F.D. et al., 2016. Mismatch of Synaptic Patterns between Neurons Produced in

977   Regeneration and during Development of the Vertebrate Retina. *Current Biology*,

978   26(17):2268–79.

979   Dorostkar, M.M. et al., 2010. Computational processing of optical measurements of neuronal

980   and synaptic activity in networks. *Journal of Neuroscience Methods*, 188(1):141–50.

981   Douglas, R.H. & McGuigan, C.M., 1989. The spectral transmission of freshwater teleost

982   ocular media-An interspecific comparison and a guide to potential ultraviolet sensitivity.

983   *Vision Research*, 29(7):871–9.

984   Dreosti, E. et al., 2009. A genetically encoded reporter of synaptic activity in vivo. *Nature*

985   *Methods*, 6(12):883–9.

986   Dunn, T.W. et al., 2016. Neural Circuits Underlying Visually Evoked Escapes in Larval

987   Zebrafish. *Neuron*, 89(3):613–28.

988   Dyakova, O. & Nordström, K., 2017. Image statistics and their processing in insect vision.

989   *Current Opinion in Insect Science*. 24:7-14.

990   Easter, Jr., S.S. & Nicola, G.N., 1996. The Development of Vision in the Zebrafish (Danio

991   rerio). *Developmental Biology*, 180(2):646–63.

992   Endeman, D., Klaassen, L.J. & Kamermans, M., 2013. Action Spectra of Zebrafish Cone

993   Photoreceptors. *PLoS ONE*, 8(7):e68540.

994   Engeszer, R.E. et al., 2007. Zebrafish in The Wild: A Review of Natural History And New

995   Notes from The Field. *Zebrafish*, 4(1):21-40.

996   Engström, K., 1960. Cone types and cone arrangements in the retina of some cyprinids.

997   *Acta Zool*, 41:277–95.

998   Enright, J.M. et al., 2015. Cyp27c1 red-shifts the spectral sensitivity of photoreceptors by

999   converting Vitamin A1 into A2. *Current Biology*, 25(23):3048–57.

1000   Euler, T. et al., 2009. Eyecup scope--optical recordings of light stimulus-evoked fluorescence

1001   signals in the retina. *Pflügers Archiv : European Journal of Physiology*, 457(6):1393–

1002   414.

1003   Euler, T. et al., 2014. Retinal Bipolar Cells: Elementary Building Blocks of Vision. *Nature*

1004   *Reviews Neuroscience*, 15:507–519.

1005   Fadool, J.M., 2003. Development of a rod photoreceptor mosaic revealed in transgenic

1006   zebrafish. *Developmental Biology*, 258(2):277–90.

1007   Famiglietti, E.V. Jr., 1983. "Starburst" amacrine cells and cholinergic neurons: mirror-

1008   symmetric on and off amacrine cells of rabbit retina. *Brain Res*, 261(1), pp.138–144.

1009   Flamarique, I.N., 2016. Diminished foraging performance of a mutant zebrafish with reduced

1010   population of ultraviolet cones. *Proceedings. Biological sciences / The Royal Society*,

1011   283(1826):20160058.

1012   Franke, K. et al., 2017. Inhibition decorrelates visual feature representations in the inner

1013   retina. *Nature*, 542(7642):439–44.

1014   Friedrich, R.W., Jacobson, G.A. & Zhu, P., 2010. Circuit Neuroscience in Zebrafish. *Current

1015   Biology*, 20(8):371-81.

1016   Goldsmith, T.H., 1994. Ultraviolet receptors and color vision: evolutionary implications and a

1017   dissonance of paradigms. *Vis.Res.*, 34(11):1479–87.

1018   Greene, M.J., Kim, J.S. & Seung, H.S., 2016. Analogous Convergence of Sustained and

1019   Transient Inputs in Parallel On and Off Pathways for Retinal Motion Computation. Cell

1020   Rep, 14(8):1892-900.

1021   Haug, M.F. et al., 2010. Visual acuity in larval zebrafish: behavior and histology. *Frontiers in

1022   Zoology*, 7:8.

1023   Helmstaedter, M. et al., 2013. Connectomic reconstruction of the inner plexiform layer in the

1024   mouse retina. *Nature*, 500(7461):168–74.

1025   Hildebrand, D.G.C. et al., 2017. Whole-brain serial-section electron microscopy in larval

1026   zebrafish. *Nature*, 545(7654):345–349.

1027   Hoon, M. et al., 2014. Functional architecture of the retina: Development and disease.

1028   *Progress in Retinal and Eye Research*, 42:44–84.

1029   Hunt, D.M. et al., 2001. Vision in the ultraviolet. *Cellular and molecular life sciences*,
1030   58(11):1583–98.

1031   Janssen, J., 1981. Searching for Zooplankton Just Outside Snell's Window.
1032   *Limmol.Oceanogr.*, 26(6):1168–71.

1033   Jerlov, N.G., 1976. *Marine Optics.* Elsevier Oceanograph Series (14), 2nd Edition.

1034   Joesch, M. & Meister, M., 2016. A neuronal circuit for colour vision based on rod–cone
1035   opponency. *Nature*, 532(7598):236-9.

1036   Johnston, J. et al., 2014. Rapid mapping of visual receptive fields by filtered back projection:
1037   application to multi-neuronal electrophysiology and imaging. *The Journal of Physiology*,
1038   592(22):4839–54.

1039   Karlsson, J., von Hofsten, J. & Olsson, P.E., 2001. Generating transparent zebrafish: a
1040   refined method to improve detection of gene expression during embryonic
1041   development. *Marine Biotechnology*, 3(6):522–7.

1042   Keller, P.J., Ahrens, M.B. & Freeman, J., 2014. Light-sheet imaging for systems
1043   neuroscience. *Nature Methods*, 12(1):27–9.

1044   Kim, J.S. et al., 2014. Space–time wiring specificity supports direction selectivity in the
1045   retina. *Nature*, 509(7500):331–6.

1046   Koskelainen, A. et al., 2000. Measurement of thermal contribution to photoreceptor
1047   sensitivity. *Nature*, 403(6766):220–3.

1048   Land, M. & Nilson, D.-E., 2012. *Animal Eyes*, Oxford University Press.

1049   Larison, K.D. & Bremiller, R., 1990. Early onset of phenotype and cell patterning in the
1050   embryonic zebrafish retina. *Development.* 109:567–76.

1051   Lewis, A. & Zhaoping, L., 2006. Are cone sensitivities determined by natural color statistics?

1052   *Journal of vision*, 6(3):285–302.

1053   Li, Y.N. et al., 2012. Bipolar cell-photoreceptor connectivity in the zebrafish (Danio rerio)

1054   retina. *The Journal of Comparative Neurology*, 520(16):3786–802.

1055   Li, Y.N., Matsui, J.I. & Dowling, J.E., 2009. Specificity of the horizontal cell-photoreceptor

1056   connections in the zebrafish (Danio rerio) retina. *The Journal of Comparative*

1057   *Neurology*, 516(5):442–53.

1058   Loew, E.R. & Dartnall, H.J.A., 1976. Vitamin A1/A2-based visual pigment mixtures in cones

1059   of the rudd. *Vision Research*, 16(9):891–6.

1060   Losey, G.S. et al., 1999. The UV visual world of fishes: a review. *Journal of Fish Biology*,

1061   54(5):921–43.

1062   Masland, R.H., 2001. The fundamental plan of the retina. *Nature Neuroscience*, 4(9):877–

1063   86.

1064   McLean, D.L. & Fetcho, J.R., 2011. Movement, technology and discovery in the zebrafish.

1065   *Current Opinion in Neurobiology*, 21(1):110–5.

1066   Mehta, B. et al., 2013. Synaptic ribbons influence the size and frequency of miniature-like

1067   evoked postsynaptic currents. *Neuron*, 77(3):516–27.

1068   Morris, D.P. et al., 1995. The attenuation of solar UV radiation in lakes and the role of

1069   dissolved organic carbon. *Limnology and Oceanography*, 40(8):1381–91.

1070   Mueller, K.P. & Neuhauss, S.C.F., 2014. Sunscreen for fish: co-option of UV light protection

1071   for camouflage. *PloS ONE*, 9(1):e87372.

1072   Muto, A. et al., 2017. Activation of the hypothalamic feeding centre upon visual prey

1073   detection. *Nature Communications*, 8:15029.

1074   Muto, A. & Kawakami, K., 2013. Prey capture in zebrafish larvae serves as a model to study

1075   cognitive functions. *Frontiers in Neural Circuits*, 7:110.

1076   Naumann, E.A. et al., 2010. Monitoring neural activity with bioluminescence during natural

1077   behavior. *Nature Neuroscience*, 13(4):513–20.

1078   Nava, S.S., An, S. & Hamil, T., 2011. Visual detection of UV cues by adult zebrafish (Danio

1079   rerio). *Journal of Vision*, 11(6):2.

1080   Nevala, N.E. et al., 2017. Mapping the Natural Visual World of Zebrafish (Danio rerio).

1081   *F1000 Posters*.

1082   Nevin, L.M., Taylor, M.R. & Baier, H., 2008. Hardwiring of fine synaptic layers in the

1083   zebrafish visual pathway. *Neural Development*, 3(1):36.

1084   Novales Flamarique, I., 2012. Opsin switch reveals function of the ultraviolet cone in fish

1085   foraging. *Proceedings of the Royal Society of London B: Biological Sciences*,

1086   280(1752):20122490.

1087   Orger, M.B., 2016. The Cellular Organization of Zebrafish Visuomotor Circuits. *Current

1088   Biology*, 26(9):377–85.

1089   Parichy, D.M., 2015. Advancing biology through a deeper understanding of zebrafish

1090   ecology and evolution. *eLife*, 4: e05635.

1091   Patterson, B.W. et al., 2013. Visually guided gradation of prey capture movements in larval

1092   zebrafish. *Journal of Experimental Biology*, 216(16):3071–83.

1093   Pita, D. et al., 2015. Vision in two cyprinid fish: implications for collective behavior. *PeerJ*,

1094   3:e1113.

1095   Preuss, S.J. et al., 2014. Classification of Object Size in Retinotectal Microcircuits. *Current

1096   Biology*. 24(20):2376-85.

1097   Robles, E., Laurell, E. & Baier, H., 2014. The Retinal Projectome Reveals Brain-Area-

1098   Specific Visual Representations Generated by Ganglion Cell Diversity. *Current Biology*,

1099   24(18):2085–96.

Rosa, J.M. et al., 2016. Crossover Inhibition Generates Sustained Visual Responses in the Inner Retina. *Neuron*, 90(2):308-19.

Ruderman, D.L., Cronin, T.W. & Chiao, C.-C., 1998. Statistics of cone responses to natural images: implications for visual coding. *Journal of the Optical Society of America A*, 15(8):2036.

Sabbah, S. et al., 2017. A retinal code for motion along the gravitational and body axes. *Nature*, 546:492-7.

Salbreux, G. et al., 2012. Coupling Mechanical Deformations and Planar Cell Polarity to Create Regular Patterns in the Zebrafish Retina S. Shvartsman, ed. *PLoS Computational Biology*, 8(8):e1002618.

Schaerer, S. & Neumeyer, C., 1996. Motion detection in goldfish investigated with the optomotor response is "color blind." *Vision Research*, 36(24):4025–34.

Schmitt, E.A. & Dowling, J.E., 1999. Early retinal development in the zebrafish, Danio rerio: light and electron microscopic analyses. *The Journal of Comparative Neurology*, 404(4):515–36.

Semmelhack, J.L. et al., 2014. A dedicated visual pathway for prey detection in larval zebrafish. *eLife*, 3:e04878.

Siebeck, U.E. & Marshall, N.J., 2001. Ocular media transmission of coral reef fish--can coral reef fish see ultraviolet light? *Vision Research*, 41(2):133–49.

Simoncelli, E.P. & Olshausen, B.A., 2001. Natural image statistics and neural representation. *Annu Rev Neurosci*, 24:1193–216.

Song, P.I., Matsui, J.I. & Dowling, J.E., 2008. Morphological types and connectivity of horizontal cells found in the adult zebrafish (Danio rerio) retina. *Journal of Comparative Neurology*, 506(2):328–38.

1124   Spence, R. et al., 2007. Diet, growth and recruitment of wild zebrafish in Bangladesh.

1125   *Journal of Fish Biology*, 71(1):304–9.

1126   Spence, R. et al., 2008. The behaviour and ecology of the zebrafish, Danio rerio. *Biological*

1127   *Reviews*, 83(1):13–34.

1128   Stell, W.K., 1967. The structure and relationships of horizontal cells and

1129   photoreceptor-bipolar synaptic complexes in goldfish retina. *American Journal of*

1130   *Anatomy*, 121(2):401–23.

1131   Suzuki, S.C. et al., 2013. Cone photoreceptor types in zebrafish are generated by symmetric

1132   terminal divisions of dedicated precursors. *Proceedings of the National Academy of*

1133   *Sciences*, 110(37):15109–14.

1134   Takechi, M., Hamaoka, T. & Kawamura, S., 2003. Fluorescence visualization of ultraviolet-

1135   sensitive cone photoreceptor development in living zebrafish. *FEBS Letters*, 553(1–

1136   2):90–4.

1137   Takechi, M. & Kawamura, S., 2005. Temporal and spatial changes in the expression pattern

1138   of multiple red and green subtype opsin genes during zebrafish development. *The*

1139   *Journal of Experimental Biology*, 208(7):1337–45.

1140   Temizer, I. et al., 2015. A Visual Pathway for Looming-Evoked Escape in Larval Zebrafish.

1141   *Current Biology*, 25(14):1823–34.

1142   Trivedi, C.A. & Bollmann, J.H., 2013. Visually driven chaining of elementary swim patterns

1143   into a goal-directed motor sequence: a virtual reality study of zebrafish prey capture.

1144   *Frontiers in Neural Circuits*, 7:86.

1145   Vitorino, M. et al., 2009. Vsx2 in the zebrafish retina: restricted lineages through

1146   derepression. *Neural Development*, 4(1):14.

1147   Wässle, H. et al., 2009. Cone contacts, mosaics, and territories of bipolar cells in the mouse

1148   retina. *The Journal of Neuroscience*, 29(1):106–17.

1149   Wässle, H., 2004. Parallel processing in the mammalian retina. *Nature Reviews*

1150   *Neuroscience*, 5(10):747–57.

1151   Webster, M.A. & Mollon, J.D., 1997. Adaptation and the color statistics of natural images.

1152   *Vision Research*, 37(23):3283–98.

1153   Wong, K.Y. & Dowling, J.E., 2005. Retinal bipolar cell input mechanisms in giant danio. III.

1154   ON-OFF bipolar cells and their color-opponent mechanisms. *Journal of*

1155   *Neurophysiology*, 94(1):265–72.

1156   Yilmaz, M. & Meister, M., 2013. Rapid Innate Defensive Responses of Mice to Looming

1157   Visual Stimuli. *Current Biology,* 23(20):2011–5.

1158   Zhang, Y. et al., 2012. The most numerous ganglion cell type of the mouse retina is a

1159   selective feature detector. *Proceedings of the National Academy of Sciences of the*

1160   *United States of America*, 109(36):e2391-8.

1161   Zhao, X.-F., Ellingsen, S. & Fjose, A., 2009. Labelling and targeted ablation of specific

1162   bipolar cell types in the zebrafish retina. *BMC Neuroscience*, 10:107.

Figure 1 - Distribution of chromatic content in the zebrafish natural visual world

a Single scene — Snell's window (Elevation 90 to -90)

b PC1 (Achromatic)

c PC2 (Chromatic)

d PC3 (Chromatic)

e n = 31 scenes — PC2+3, PC3 — Variance expl. (%) 0 5 10 15

f XY-scan mirrors, Spectrometer, Pinhole

g Mean light — Power (norm.) — Sky, Water — Wavelength (nm) 300 400 500 600 700

h U B G R — Absorption — Water — Wavelength (nm) 300 400 500 600 700

i Elevation (°) 30 0 -30

j R G B U

l PC2+3+4, PC4, PC3+4 — Variance expl. (%) 0 10 20 30 40

k RGBU — Loadings 1 to -1 — PC1 PC2 PC3 PC4

m Colour Statistics — Achromatic, Chromatic

n Behavioural demands — Prey-capture, UV-dark silhouettes, "Strike zone"

Figure 2 - Anisotropic retinal ultrastructure

a

3D confocal stack | 2D projection | Cell-detection | 3D projection | Density

100 μm

D
N — T
V

b

R | G | B | U | rod

c

"Strike zone"

PRs mm^{-2} (*10^4)

3

2

U
R
G
rod
B

1

0

Up   SZ   Down   Horizon

d

"Strike zone"

Up

U
G
B

R

Down

Outward horizon

2*10^4 PR mm^{-2}

e

"Up"
"Strike-zone"
"Outward horizon"
"Down"

f

RibeyeA:SyGCaMP6
ChAT, PKCa

Looking down

OPL
INL
IPL
GCL

Outward horizon | Forward horizon

"Strike zone"

D
N — T
V

Looking up

g₁ Looking up | **g₂**

h₁ "Strike zone" | **h₂**

i₁ Looking down | **i₂**

j₁ Outward horizon | **j₂**

k

IPL width (μm)

15

10

5

Up   SZ   Down   Horizon

l

IPL depth (%)

GFP
PKCa
ChAT

100
50
0

Up   SZ   Down   Horizon

Figure 3 - Surveying inner retinal chromatic responses *in vivo*

a

IPL depth (%)

100

0

100

0

1

2

b

1

2

10 sd

5 s

c

1

2

20 sd

0.5 s

d Outward horizon

IPL depth (%)

Red   Green   Blue   UV

100

0

On Off   **On** Off   **On** Off   **On** Off

e

Achromatic   Opponent   Other   All

On Off   **On/Off**   On Off

f "Strike zone (SZ)"

IPL depth (%)

100

0

g

h

Fraction of terminals

0.6

0

On   Off

Up   SZ   Down   Horizon

i

On   Off

Up   SZ   Down   Horizon

j

On   Off

Up   SZ   Down   Horizon

k

On   Off

Up   SZ   Down   Horizon

Figure 4 - The functional organisation of the larval zebrafish eye

n = 4,099 / 6,565 Terminals, 115 Scans, 12 fish

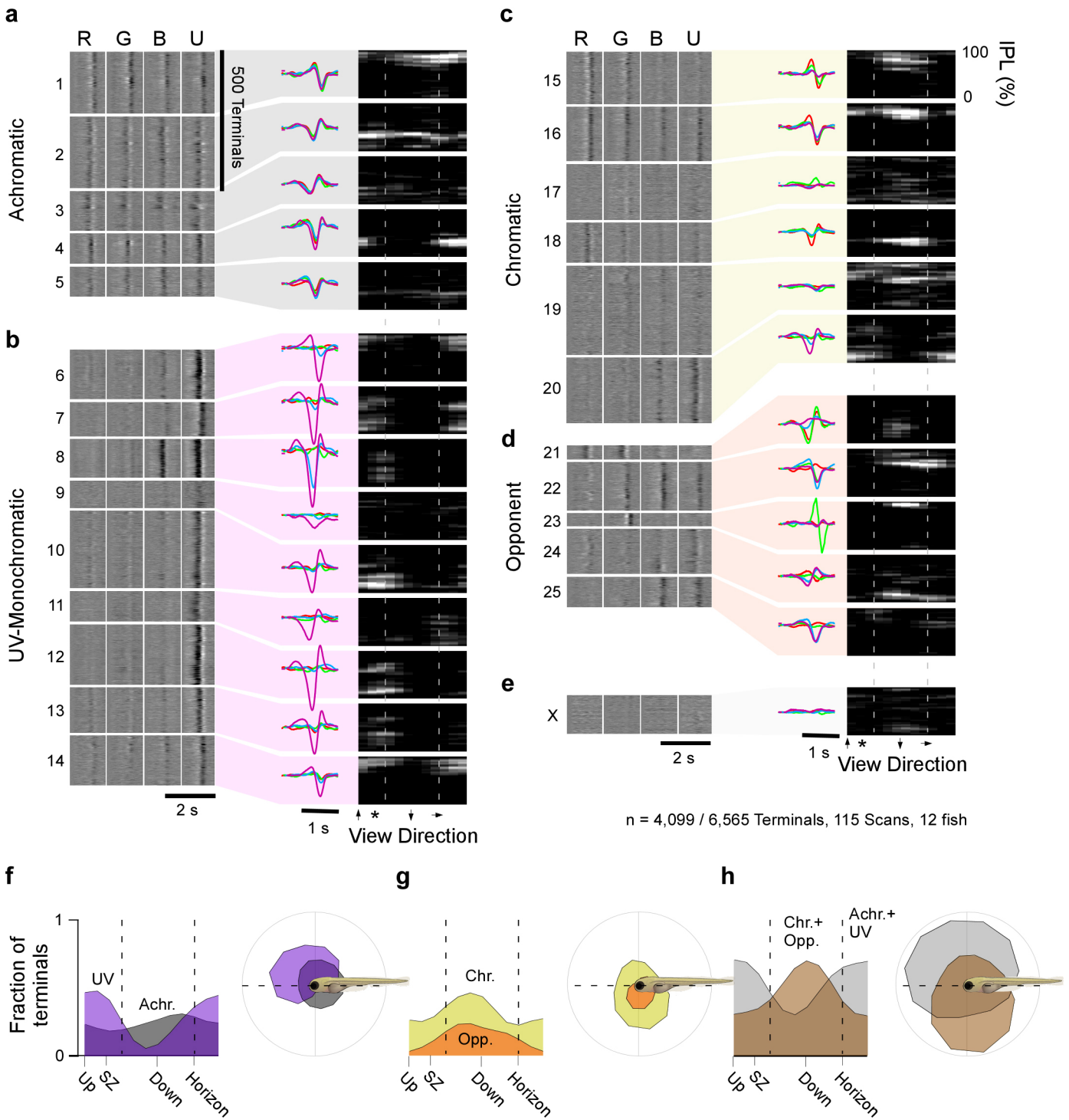# Figure 5 - Distribution of function across the IPL

a
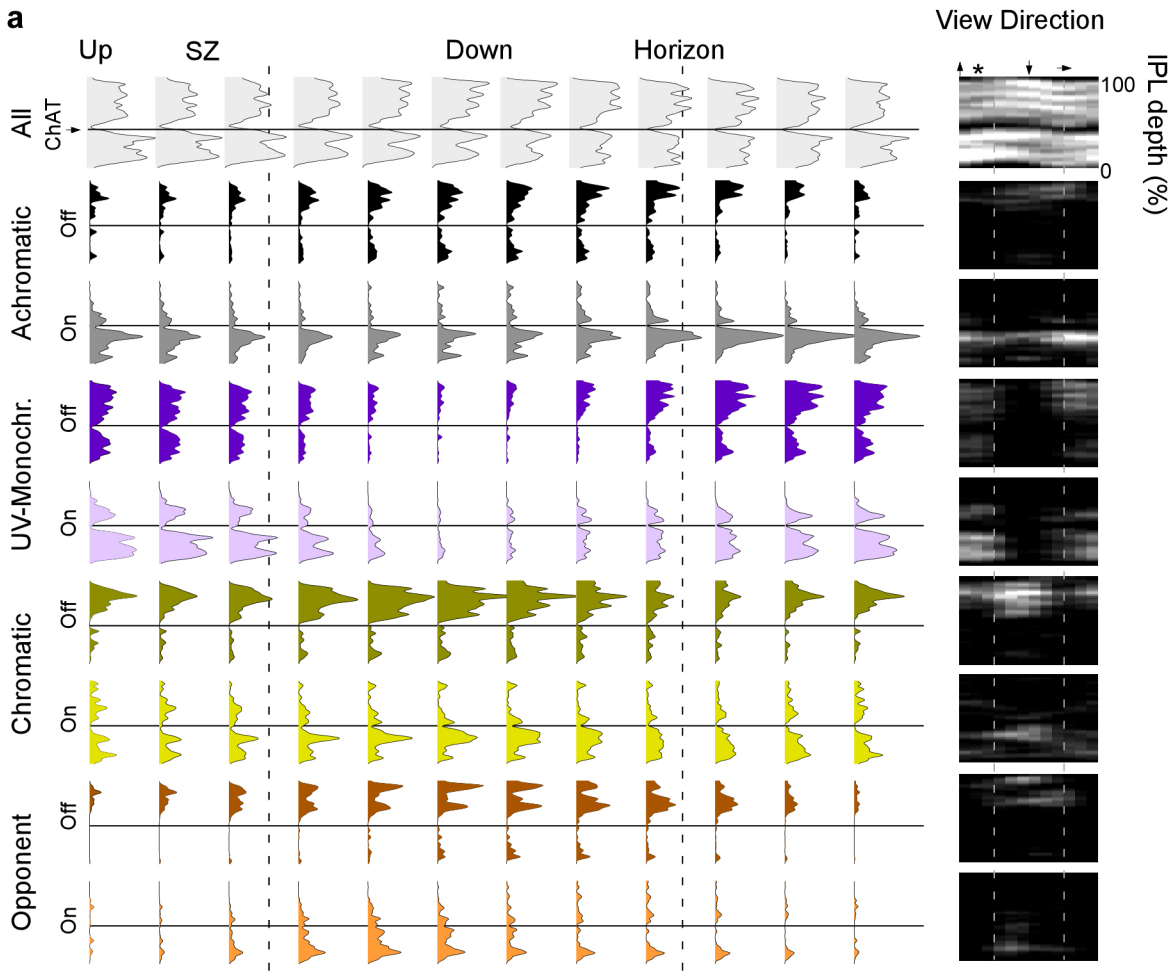
Up   SZ   Down   Horizon

View Direction

All
ChAT

Achromatic — Off / On

UV-Monochr. — Off / On

Chromatic — Off / On

Opponent — Off / On

IPL depth (%)   100   0

b₁ Up   **b₂** Strike Zone   **b₃** Down   **b₄** Horizon

Anatomical layers   1 2 3 4 5 6

c   Achromatic   UV   Chromatic   Opponent   IPL depth (%)   100   0
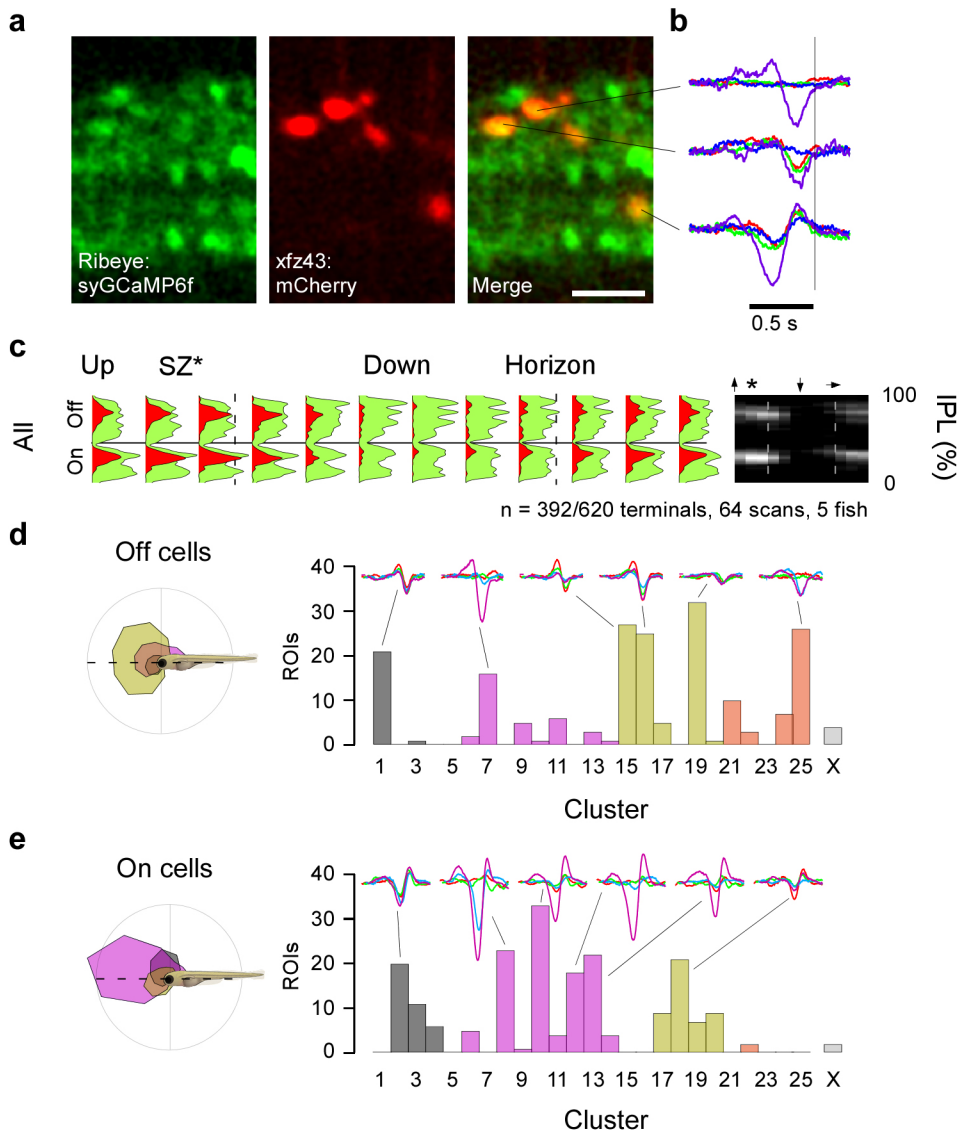
Figure 6 - Distribution of genetically defined BC-types

a

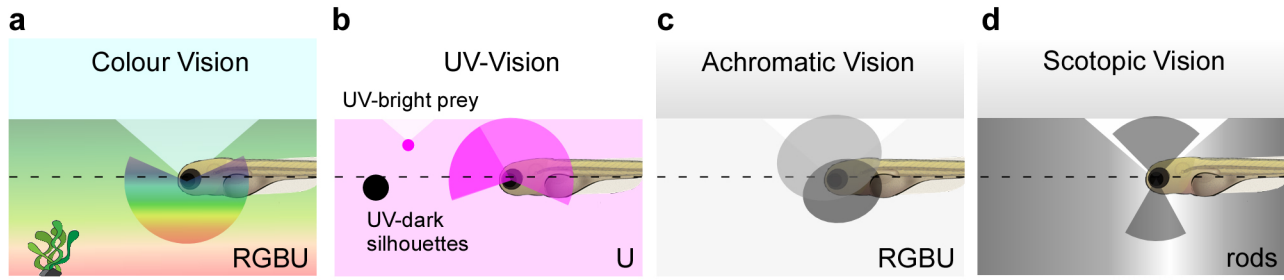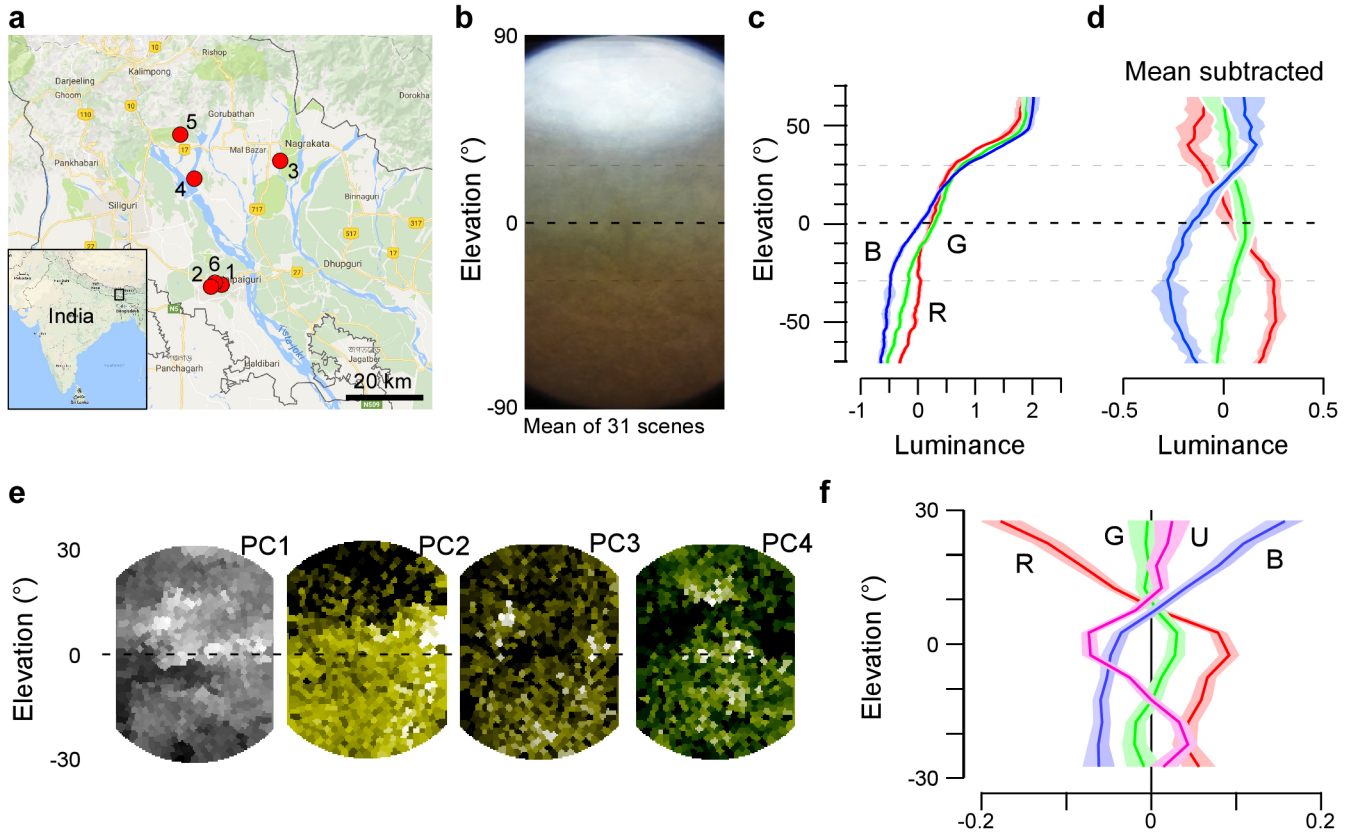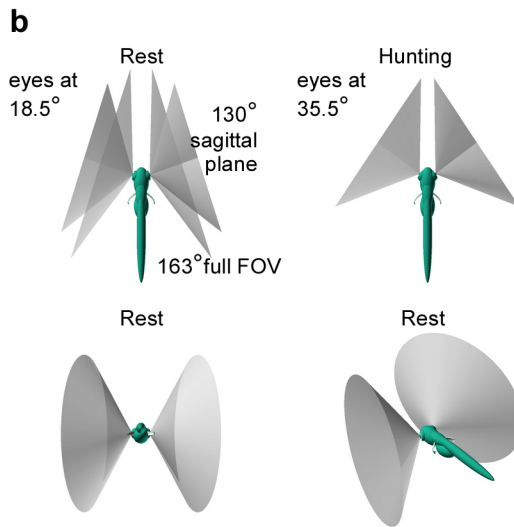
Ribeye: syGCaMP6f   xfz43: mCherry   Merge

b

0.5 s

c

Up   SZ*   Down   Horizon

All   Off   On

* ↑ ↓ →   100   IPL (%)   0

n = 392/620 terminals, 64 scans, 5 fish

d

Off cells

ROIs
40
30
20
10
0

1 3 5 7 9 11 13 15 17 19 21 23 25 X

Cluster

e

On cells

ROIs
40
30
20
10
0

1 3 5 7 9 11 13 15 17 19 21 23 25 X

Cluster

Figure 7 - Summary

a Colour Vision — RGBU

b UV-Vision — U
UV-bright prey
UV-dark silhouettes

c Achromatic Vision — RGBU

d Scotopic Vision — rods

Supplementary Figure 1

a (map with locations 1–6 marked; inset showing India; scale bar 20 km)

b Mean of 31 scenes

c Elevation (°) vs Luminance; curves labeled B, G, R

d Mean subtracted; Elevation (°) vs Luminance

e Elevation (°); PC1, PC2, PC3, PC4

f Elevation (°); curves labeled R, G, U, B

Supplementary Figure 2

a

b

a

b

c

d

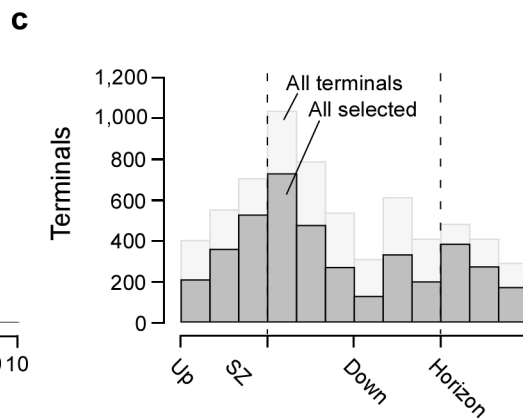## Supplementary Figure 4

Supplementary Data Sheet 1

	R	G	B	U	RGB	PC 2-4	
							Scan 1
							Scan 2
							Scan 3
							Scan 4
							Scan 5
							Scan 6
							Scan 7
							Scan 8
							Scan 9
							Scan 10

Field site 1

Field site 2

Supplementary Data Sheet 2

	R	G	B	U	RGB	PC 2-4	
							Scan 11
							Scan 12
							Scan 13
							Scan 14
							Scan 15
							Scan 16
							Scan 17
							Scan 18
							Scan 19
							Scan 20
							Scan 21

Field site 3

Field site 4

Supplementary Data Sheet 3

	R	G	B	U	RGB	PC 2-4	
							Scan 22
							Scan 23
							Scan 24
							Scan 25
							Scan 26
							Scan 27
							Scan 28
							Scan 29
							Scan 30
							Scan 31

Field site 5

Field site 6